EVALUATING THE BENEFITS OF USING LONGWAVE INFRARED AND MILLIMETER/SUB-MILLIMETER BANDS TO EXPLORE ICE CLOUD CHARACTERISTICS THROUGH POLARIZED VECTOR RADIATIVE TRANSFER SIMULATIONS

A Thesis

by

JAMES JOSEPH COY JR.

Submitted to the Office of Graduate and Professional Studies of
Texas A&M University
In partial fulfillment of the requirements for the degree of

MASTER OF SCIENCE

Chair of Committee,	Ping Yang
Co-Chair of Committee,	R. Saravanan
Committee Members,	Kenneth Bowman
	Anthony Filippi
Head of Department,	R. Saravanan

May 2019

Major Subject: Atmospheric Sciences

ABSTRACT

A comprehensive study on evaluating the usefulness of relatively high frequency millimeter/sub-millimeter (mm/sub-mm) bands (> 150 GHz) and longwave infrared (LWIR) atmospheric window bands to infer ice cloud properties will be conducted for this thesis. A sizable amount of mm/sub-mm bands have been considered from radiometric and polarimetric studies to be useful for observing ice clouds with lower mm/sub-mm wavelengths (higher frequencies) being able to observe even optically thin cirrus. The LWIR atmospheric window has been thoroughly investigated for their feasibility to also observe ice clouds, especially optically thin cirrus. However, there have not been many studies conducted using several of these relatively high frequency bands or polarimetric LWIR observations to infer ice cloud properties. There have also not been many studies using simulated ice clouds composed of the latest ice particle habit mixtures and single-scattering properties. The single-scattering property databases have considered dependencies such as surface roughness and ambient temperature.

This thesis will be focusing on performing simulations on ice clouds using the wavelengths of 440.87 μm (680 GHz), 707.06 μm (424 GHz), 922.44 μm (325 GHz), 1362.69 μm (220 GHz), and 1638.21 μm (183 GHz) for the mm/sub-mm regime and 8.6 μm, 10.6 μm, and 12 μm wavelengths of the IR regime. The Atmospheric Radiative Transfer Model (ARTS) will be used to conduct the simulations for 1D atmospheres corresponding to the tropical region. The ice cloud simulations were performed for combinations of ice water path (IWP) and effective diameter (D_{eff}). IWP and D_{eff} look-up tables (LUT) were created in order to evaluate the feasibility of retrieving these values. These LUTs were then used to retrieve IWP and D_{eff} for the 1D vertically heterogeneous ice cloud scenarios which will be using 3D ice clouds

produced by Cloudgen – a stochastic cloud generator. The brightness temperature (T_b) parameters that were used to infer the cloud properties are the split-window technique (BTD), brightness temperature depression relative to clear-sky (ΔT_b), and the polarization difference (PD).

ACKNOWLEDGEMENTS

I would like to thank my committee chair, Dr. Yang, and my committee members, Dr. Saravanan, Dr. Bowman, and Dr. Filippi, for their guidance and support throughout the course of this research.

Thanks also goes to my colleagues for helping me with certain aspects of my research that required better understanding and/or further analysis. I would also like to thank my atmospheric sciences professors from courses I had previously taken as an undergraduate and graduate student for making my 7 years at Texas A&M University a fantastic experience.

Finally, thanks to my family for their encouragement and support throughout my time at Texas A&M University.

CONTRIBUTORS AND FUNDING SOURCES

Contributors

This work was supervised by a thesis committee consisting of Professor Ping Yang (chair), R. Saravanan (co-chair), and Kenneth Bowman of the Department of Atmospheric Sciences and Professor Anthony Filippi of the Department of Geography.

All work conducted for the thesis was completed by the student independently.

Funding Sources

Graduate study was supported by a graduate research assistantship from Texas A&M University.

This work was done as part of the National Aeronautics and Space Administration's (NASA) Compact Sub-mm Wave and Longwave Infrared Polarimeters for Cirrus Ice Properties Project (SWIRP) under Grant Number NNX17AJ38G.

NOMENCLATURE

ΔT_b	Brightness Temperature Depression Relative to Clear-Sky
ARTS	Atmospheric Radiative Transfer Simulator
BTD	Brightness Temperature Difference
D_{eff}	Effective Diameter
IGHM	Improved General Habit Mixture
IWC	Ice Water Content
IWP	Ice Water Path
LUT	Lookup Table
LWIR	Longwave Infrared
MC6	MODIS Collection-6
Mm/sub-mm	Millimeter/sub-millimeter
MODIS	Moderate Resolution Imaging Spectroradiometer
PD	Polarization Difference
T_b	Brightness Temperature
THM	Two-Habit Model

TABLE OF CONTENTS

Page

ABSTRACT ii

ACKNOWLEDGEMENTS iv

CONTRIBUTORS AND FUNDING SOURCES v

NOMENCLATURE vi

TABLE OF CONTENTS vii

LIST OF FIGURES ix

1. INTRODUCTION AND BACKGROUND 1

    1.1 Topic and Purpose 2
    1.2 Literature Review 3
    1.3 Theoretical Concerns 8
    1.4 Outline of Study 9

2. ATMOSPHERIC RADIATIVE TRANSFER SIMULATOR (ARTS) AND CLOUDGEN DESCRIPTION 10

    2.1 ARTS Simulated Sensor Settings 11
    2.2 ARTS Simulated Cloudbox Settings and Cloudgen 12
    2.3 ARTS Simulated Atmosphere Settings 14

3. THE ICE CLOUD MODEL 15

    3.1 Ice Particle Properties Database 15
    3.2 Ice Particle Size Distribution: D_{eff}, IWP, and Particle Number Density Calculation 16
    3.3 Ice Particle Habit Mixtures 19

4. BRIGHTNESS TEMPERATURE PARAMETERS AND LUT METHODOLOGY 22

    4.1 LWIR Split-Window Technique (BTD) 23
    4.2 Mm/sub-mm Brightness Temperature Relative to Clear-Sky (ΔT_b) 23
    4.3 Polarization Difference (PD) 24
    4.4 IWP and D_{eff} Isoline LUT Methodology 24

Page

5. RESULTS 28

5.1 Sensitivity Analyses and LUTs Discussion 28
5.2 2D LUT Retrieval Results 52

6. SUMMARY AND CONCLUSIONS 60

6.1 Summary 60
6.2 Conclusions 61

REFERENCES 64

LIST OF FIGURES

FIGURE Page

1 Schematic of a 1D atmosphere implemented in ARTS. The radius of the geoid, the surface and all pressure levels are constant around the globe. The extension of the cloud box is either from the surface up to a pressure level, or between two pressure levels (shown in the figure). The surface (ground) must be above the lowermost pressure level. Image adapted from Buehler et al. 2017. 10

2 Example 2D slice of stochastic cirrus clouds represented as IWC (gm^{-3}) outputted by Cloudgen. 13

3 Pressure (bottom x-axis) and temperature (top x-axis) profiles used by ARTS to simulate an atmosphere similar to what is typically observed in a tropical atmosphere. 14

4 IGHM consisting of 9 ice particle habits with fractions changing linearly as size changes. It can be seen the aggregates mainly populate large particle sizes. Reprinted from Baum et al. 2011. **© American Meteorological Society. Used with permission.** 20

5 The THM used by Liu et al. 2014 with ice particle habit fraction as a function of particle size. It can be seen that the hexagonal 8-column aggregate (agg. 8 sol. column) eventually dominates the habit mixture as particle size increases. Image adapted from Liu et al. 2014. 21

6 An example 2D IWP and D_{eff} isoline LUT. The LUT should typically exhibit a grid-like format where IWP and D_{eff} isolines are organized by descending/ ascending values. The isolines are plotted with respect to corresponding brightness temperature parameters (BTD/ΔT_b/PD) of 2 or more wavelengths. 25

7 Contour and line plot sets representing sensitivities of 8.6 μm – 10.6 μm BTDs with respect to IWP and D_{eff} at 53.5° and 0° (nadir) viewing angles. (A, E), (B, F), and (C, G) are contour plots displaying $\delta BTD/\delta D_{eff}$ for MC6, IGHM, and THM. (D, H) are D_{eff} vs. BTD plots for IWPs of 10 gm^{-2}, 100 gm^{-2}, 260 gm^{-2}, and 500 gm^{-2}. 29

8 Contour and line plot sets representing sensitivities of 8.6 μm – 12 μm BTDs with respect to IWP and D_{eff} at 53.5° and 0° (nadir) viewing angles. (A, E), (B, F), and (C, G) are contour plots displaying $\delta BTD/\delta D_{eff}$ for MC6, IGHM, and THM. (D, H) are D_{eff} vs. BTD plots for IWPs of 10 gm^{-2}, 100 gm^{-2}, 260 gm^{-2}, and 500 gm^{-2}. 30

FIGURE Page

9 (A, D) MC6 IWP (red lines) and D_{eff} (blue lines) isoline LUT plots of 8.6 μm – 12 μm BTDs with respect to 12 μm T_bs at 53.5° and 0° (nadir) viewing angles. (B, E) contour plot of IGHM unit deviation from MC6 fitted in between the LUT isolines of (A, D). (C, F) contour plot of IGHM unit deviation from MC6 fitted in between the LUT isolines of (A, D)..... 32

10 Contour and line plot sets representing sensitivities of 183 GHz (1636 μm) ΔT_bs with respect to IWP and D_{eff} at 53.5° and 0° (nadir) viewing angles. (A, E), (B, F), and (C, G) are contour plots displaying $\delta \Delta T_b / \delta D_{eff}$ for MC6, IGHM, and THM. (D, H) are D_{eff} vs. ΔT_b plots for IWPs of 10 gm^{-2}, 100 gm^{-2}, 260 gm^{-2}, and 500 gm^{-2}. 34

11 Contour and line plot sets representing sensitivities of 220 GHz (1363 μm) ΔT_bs with respect to IWP and D_{eff} at 53.5° and 0° (nadir) viewing angles. (A, E), (B, F), and (C, G) are contour plots displaying $\delta \Delta T_b / \delta D_{eff}$ for MC6, IGHM, and THM. (D, H) are D_{eff} vs. ΔT_b plots for IWPs of 10 gm^{-2}, 100 gm^{-2}, 260 gm^{-2}, and 500 gm^{-2}. 35

12 Contour and line plot sets representing sensitivities of 325 GHz (922 μm) ΔT_bs with respect to IWP and D_{eff} at 53.5° and 0° (nadir) viewing angles. (A, E), (B, F), and (C, G) are contour plots displaying $\delta \Delta T_b / \delta D_{eff}$ for MC6, IGHM, and THM. (D, H) are D_{eff} vs. ΔT_b plots for IWPs of 10 gm^{-2}, 100 gm^{-2}, 260 gm^{-2}, and 500 gm^{-2}. 37

13 Contour and line plot sets representing sensitivities of 680 GHz (441 μm) ΔT_bs with respect to IWP and D_{eff} at 53.5° and 0° (nadir) viewing angles. (A, E), (B, F), and (C, G) are contour plots displaying $\delta \Delta T_b / \delta D_{eff}$ for MC6, IGHM, and THM. (D, H) are D_{eff} vs. ΔT_b plots for IWPs of 10 gm^{-2}, 100 gm^{-2}, 260 gm^{-2}, and 500 gm^{-2}. 38

14 (A, D) MC6 IWP (red lines) and D_{eff} (blue lines) isoline LUT plots of 680 GHz ΔT_bs with respect to 220 GHz/183 GHz ΔT_b ratio at 53.5° and 0° (nadir) viewing angles. (B, E) contour plot of IGHM unit deviation from MC6 fitted in between the LUT isolines of (A, D). (C, F) contour plot of IGHM unit deviation from MC6 fitted in between the LUT isolines of (A, D). 40

15 Contour and line plot sets representing sensitivities of 8.6 μm (A – D), 10.6 μm (E – H), and 12 μm (I – L) PDs with respect to IWP and D_{eff} at the 53.5° viewing angle. (A, E, I), (B, F, J), and (C, G, K) are contour plots displaying $\delta PD / \delta D_{eff}$ for MC6, IGHM, and THM. (D, H, L) are D_{eff} vs. PD plots for IWPs of 10 gm^{-2}, 100 gm^{-2}, 260 gm^{-2}, and 500 gm^{-2}..... 42

FIGURE Page

16 Contour and line plot sets representing sensitivities of 183 GHz (1636 μm) and 220 GHz (1363 μm) PDs with respect to IWP and D_{eff} at the 53.5° viewing angle. (A, E), (B, F), and (C, G) are contour plots displaying $\delta PD/\delta D_{eff}$ for MC6, IGHM, and THM. (D, H) are D_{eff} vs. ΔT_b plots for IWPs of 10 gm^{-2}, 100 gm^{-2}, 260 gm^{-2}, and 500 gm^{-2}. 44

17 Contour and line plot sets representing sensitivities of 325 GHz (922 μm) and 680 GHz (441 μm) PDs with respect to IWP and D_{eff} at the 53.5° viewing angle. (A, E), (B, F), and (C, G) are contour plots displaying $\delta PD/\delta D_{eff}$ for MC6, IGHM, and THM. (D, H) are D_{eff} vs. ΔT_b plots for IWPs of 10 gm^{-2}, 100 gm^{-2}, 260 gm^{-2}, and 500 gm^{-2}. 45

18 (A) MC6 IWP (red lines) and D_{eff} (blue lines) isoline LUT plots of 183 GHz PDs with respect to 220 GHz PDs for the 53.5° viewing angle. (B) Contour plot of IGHM unit deviation from MC6 fitted in between the LUT isolines of (A). (C) Contour plot of IGHM unit deviation from MC6 fitted in between the LUT isolines of (A). 48

19 (A) MC6 IWP (red lines) and D_{eff} (blue lines) isoline LUT plots of 220 GHz ΔT_bs with respect to 12 μm PDs for the 53.5° viewing angle. (B) Contour plot of IGHM unit deviation from MC6 fitted in between the LUT isolines of (A). (C) Contour plot of IGHM unit deviation from MC6 fitted in between the LUT isolines of (A). 49

20 Contour and line plot sets representing sensitivities of 424 GHz (669 μm) ΔT_bs (A – D) and PDs (E – H) with respect to IWP and D_{eff} at the 53.5° viewing angle. (A, E), (B, F), and (C, G) are contour plots displaying $\delta \Delta T_b/\delta D_{eff}$ and $\delta PD/\delta D_{eff}$ for MC6, IGHM, and THM. (D, H) are D_{eff} vs. ΔT_b and D_{eff} vs. PD plots for IWPs of 10 gm^{-2}, 100 gm^{-2}, 260 gm^{-2}, and 500 gm^{-2}. 50

21 (A) IWPs for the Cloudgen retrieval scenario with each pixel representing a 1 km by 1 km square and a single retrieval case. (B) IWP distribution bar graph with each bar representing a 50 gm^{-2} interval. (C) D_{eff}s for the Cloudgen retrieval scenario with each pixel representing a 1 km by 1 km square and a single retrieval case. (D) D_{eff} distribution bar graph with each bar representing a 50 μm interval. *N* represents the total number of retrieval cases while N_{true} represents the number of retrieval cases considered for analysis due IWPs > 10 gm^{-2} and D_{eff} > 10 μm. .. 51

FIGURE Page

22 IWP (A) and D_{eff} (B) scatter plots of each retrieval case corresponding to the true values and the retrieved values from the 8.6 μm – 12 μm BTD vs. 12 μm T_b LUT (Figure 9A). *Std. dev* represents the standard deviation of the retrievals and *mean % err.* represents the average percentage error of the D_{eff} retrievals. The black diagonal line represents the line of 0% retrieval error. 53

23 IWP (A) and D_{eff} (B) scatter plots of each retrieval case corresponding to the true values and the retrieved values from the 220 GHz/183 GHz ΔT_b ratio vs. 680 ΔT_b LUT (Figure 14A). *Std. dev* represents the standard deviation of the retrievals and *mean % err.* represents the average percentage error of the retrievals. The black diagonal line represents the line of 0% retrieval error. 54

24 IWP (A) and D_{eff} (B) scatter plots of each retrieval case corresponding to the true values and the retrieved values from the 220 GHz PD vs. 183 GHz PD LUT (Figure 18A). *Std. dev* represents the standard deviation of the retrievals and *mean % err.* represents the average percentage error of the retrievals. The black diagonal line represents the line of 0% retrieval error. 56

25 IWP (A) and D_{eff} (B) scatter plots of each retrieval case corresponding to the true values and the retrieved values from the 12 μm PD vs 220 GHz ΔT_b LUT (Figure 19A). *Std. dev* represents the standard deviation of the retrievals and *mean % err.* represents the average percentage error of the retrievals. The black diagonal line represents the line of 0% retrieval error. 57

1. INTRODUCTION AND BACKGROUND

Ice clouds have been a source of uncertainty among climate models and are typically disregarded despite being globally distributed by covering more than 50% of the Earth's surface (Wang et al. 1996) and known to have significant effects on the radiative transfer budget (Liou et al. 1986). Ice clouds can create a greenhouse effect by trapping infrared (IR) radiation from the Earth from escaping to space. Ice clouds also typically increase albedo which creates a cooling effect by reflecting shortwave radiation from the Sun back to space. The net radiative effects of ice clouds greatly depend on their macrophysical and microphysical characteristics, including cloud horizontal/vertical structure, ice water content (IWC), and ice particle size. In order to better understand how the presence of ice clouds affect the radiative forcing of the climate, numerous studies have been conducted to understand their ice particle compositions (Yang et al. 2005; Yang et al. 2013). These results led to the creation of ice crystal optical property databases to be used in radiative transfer models in order to discover the properties of ice clouds such as cloud ice water path (IWP) and ice particle effective diameter (D_{eff}) (Weng and Grody, 2000; Wang et al. 2011).

There has been attention focused on the usefulness of mm/sub-mm microwave bands for observing ice clouds due to the fact that they are largely opaque to the atmospheric water vapor. This prevents noise from of the lower atmosphere and surface and allows for clear observations of ice clouds. For cirrus clouds, the brightness temperature depressions caused by ice particle scattering have shown to be proportional to its IWP when using mm/sub-mm bands (Liu and Carry, 2000). Studies have also shown the potential of polarization measurements using mm/sub-mm bands to determine cirrus cloud microphysical properties (J. Miao et al. 2003).

LWIR bands are particularly useful for observing optically thick clouds, which occur at typically lower, warmer altitudes which mostly contains liquid clouds. With the exception of convective clouds, pure ice clouds (e.g. cirrus), which are typically observed in higher, colder altitudes, are difficult to detect due to emission closely resembling clear-sky emission (Shaw and Nugent, 2013). However, methods have been used to detect cirrus clouds and even infer their microphysical properties such as the split-window technique (Inoue et al. 1985).

1.1. Topic and Purpose

The radiometric and polarimetric potential of mm/sub-mm bands being able to observe ice clouds and the lack of polarized ice cloud LWIR observations provides a good source of study. Numerous mm/sub-mm bands have been considered to be in some way useful in detecting ice clouds and determining their microphysical properties (Liu and Curry, 2000; J. Miao et al. 2003). While high-mm (low frequency) bands (< 150 GHz) are useful for atmospheric soundings and observations of liquid and precipitating clouds (Liu and Curry, 1993), low mm/sub-mm (high frequency) bands are needed to observe ice clouds, especially thin cirrus (Liu and Curry, 2000). For this study, frequencies greater than 150 GHz were used in observing simulated ice clouds for 1D atmospheres though the use of ARTS (Atmospheric Radiative Transfer Simulator): 440.87 μm (680 GHz), 707.06 μm (424 GHz), 922.44 μm (325 GHz), 1362.69 μm (220 GHz), and 1638.21 μm (183 GHz).

LWIR bands, namely 8.6 μm, 10.6 μm, and 12 μm, are some of the commonly used atmospheric window bands in the determination of cloud parameters. Split-window techniques involving the differences between these bands such as 8.6 μm – 10.6 μm have been used to identify cloud type including ice clouds (Inoue et al. 1985; Prabhakara et al. 1988). Despite there being studies about the uses of these bands to infer ice cloud properties there have yet to be

studies utilizing polarized LWIR bands to also accomplish the same goal. For this study, with the addition of using the split-window technique, polarized LWIR simulations of the 8.6 μm, 10.6 μm, and 12 μm wavelengths were conducted in order to evaluate their use for inferring ice cloud properties.

1.2. Literature Review

1.2.1. Microwave Radiative Transfer of Ice Clouds

A number of high frequency (low mm/sub-mm) microwave bands have been investigated for their feasibility to infer ice cloud properties. Sensitivities to ice clouds tend to increase as higher frequencies are used, even to the point where thin cirrus are easily detectable (Evans and Stephens, 1995ab; Liu and Curry, 2000). Evans and Stephens et al. (1995b) computed T_b at 85.5 GHz, 157 GHz, 220 GHz, and 340 GHz for 3 km-thick tropical and midlatitude cirrus clouds composed of various particle shapes and size distributions. ΔT_bs and IWP ratios (ΔT_b/IWP), adjacent frequency ΔT_b ratios, and horizontally and vertically polarized T_b (T_{bh} and T_{bv}) ratios (T_{bh}/ T_{bv}) were calculated. ΔT_b/IWP ratios indicated high sensitivity for average size distributions (or D_{eff}) and higher frequencies. Ratios of ΔT_bs at adjacent frequencies were also sensitive to D_{eff} but were ambiguous to the smallest and largest particles used in the study. T_{bh}/ T_{bv} ratio was sensitive to particle shape by their aspect ratio but the sensitivity range was significantly reduced at a 49° viewing zenith angle due to the reduction of T_{bv}. These discoveries gave ideas for the development of a cirrus microwave remote sensing algorithm in order to retrieve ice cloud D_{eff}, IWP, and particle shape (Evans and Stephens, 1995b).

Liu and Curry et al. (2000) investigated a method to simultaneously retrieve IWP and D_{eff} by using 150 GHz and 220 GHz bands from nonprecipitating clouds including ice clouds and cirrus. The study used the adjacent frequency ΔT_b ratio (ΔT_{b220}/ΔT_{b150}) used by Evans and

Stephens et al. along with ΔT_b for 220 GHz to create a LUT made up of IWP and D_{eff} isolines. Percentage root-mean-square errors were also calculated for instances of IWPs and D_{eff}s based on model uncertainties. It was found that percentage errors increased above 25% for IWP < 200 gm^{-2} and D_{eff} < 200 μm which are typically representative of thin cirrus. Frequencies greater than 220 GHz were recommended to accurately retrieve microphysical properties from thin cirrus (Liu and Curry, 2000).

With the usefulness of high frequency (lower mm/sub-mm) microwave bands becoming apparent, their use in polarization measurements have also attracted attention. J. Miao et al. (2003) investigated this by conducting polarization measurements of simulated cirrus clouds for seven frequencies: 90, 157, 220, 340, 463, 683, and 874 GHz. A parameter known as the PD, the difference between T_{bh} and T_{bv}, with respect to cloud median mass equivalent diameter (or D_{eff}) was used to determine the polarization potential of the frequencies. The results for a cirrus cloud composed of nearly spherical particles revealed that the PD resonance peak decreases in magnitude and shifts to larger D_{eff}s as frequency increases. PDs were also affected by the particle aspect ratio and orientation with overall values increasing in magnitude and D_{eff} range as aspect ratio increases and orientation becomes horizontal rather than random which indicates that PD is also sensitive to ice particle shape. It is clearly shown that higher microwave frequencies contain a great deal of thin cirrus polarization information while lower frequencies become unreliable (J. Miao et al. 2003). Despite this, J. Miao et al. pointed out that these results were from a simplified radiative transfer model that ignored the water vapor screening effect in the layer above the clouds and the omitted of the polarization signal from the ground surface. More realistic radiative transfer simulations needed to be performed to confirm these results.

Davis et al. (2007) performed 1D and 3D polarized radiative transfer simulations utilizing ARTS and 3D ice water content (IWC) fields generated from 2D (height, time) cloud radar observations to represent midlatitude ice clouds. This allowed for the generation of inhomogeneous ice clouds based on IWCs varying with height, latitude, and longitude using Cloudgen. Simulated observations for 3 satellite-borne instruments operating in the mm/sub-mm range were used for the scenarios at 190.31 GHz, 334.65 GHz, and 664 GHz. Horizontally aligned oblate spheroids with 1.3 and 3 aspect ratios were used for the cloud particles. Comparisons between the 1D and 3D simulations involving observed radiance depressions ($\Delta I = I_{cloudy} - I_{clear}$) and PDs revealed that the 1D simulations overestimated the magnitude of both measurements with it increasing with increasing cloud optical path. Davis et al. demonstrated that the cause of the differences between the observed radiances was the beamfilling effect. The effect is caused by averaging the inhomogeneities of the cloud in the field of view, where some parts of the field of view have high enough optical path to be in the radiative transfer regime. The beamfilling effect was found to be the main source of retrieval error of rainfall rates. Despite this, the contribution of 3D radiative transfer effects in the simulations were not significant in the few scenarios that were studied and a more complete investigation of the 1D/3D radiance and polarization differences needed to be performed (Davis et al. 2007).

1.2.2. Infrared Radiative Transfer of Ice Clouds

Although infrared bands are primarily used to observe thermal radiation of optically thick clouds, methods have been implemented to allow for the observation of optically thin clouds (e.g. cirrus). The channels within the 8 μm – 13 μm LWIR atmospheric window have become part of the methods developed to infer single-scattering properties of relatively thin clouds (Inoue et al. 1985). In particular, the split-window technique involving bands at or around 8.5

μm, 11 μm, and 12 μm has been commonly utilized to accomplish this task. The split-window technique is the difference between the T_bs of a "clean" window IR band (little absorption of water vapor) and a "dirty" window (moderate absorption of water vapor) (e.g. 10.6 μm and 12 μm). It is based on the fact that the absorption characteristics of ice are different at 10.6 μm and 12 μm wavelengths (Prabhakara et al. 1988). 8 μm – 9 μm wavelengths are primarily used for inferring cloud top phase, volcanic dust cloud detection, and thin cirrus detection.

Dubuisson et al. (2008) investigated the sensitivity of simulated brightness temperatures associated with radiances at the surface and the top of the atmosphere for 8.7 μm, 10.6 μm, and 12 μm channels. For space-borne simulations it was found that using the 10.6 μm –12 μm split-window technique were sensitive to small D_{eff}s (< 40 μm) for optical depths between 0.3 and 8. This allows the retrieval for cloud properties with rather low uncertainty (< ± 25%) for D_{eff}, optical thickness, and IWP. The uncertainties were due to particle habit and size distribution (monodisperse, monomodal gamma, and bimodal). The use of the third channel, 8.7 μm, allowed for the improvement of determination of D_{eff} and optical thickness due to the fact that 8.7 μm T_bs are greatly impacted by scattering, especially for small D_{eff}s (< 100 μm) and optical thickness (< 10). Scattering has a smaller effect at 10.6 μm also for relatively small D_{eff}s. Ground simulations showed that T_b values changed noticeably for different atmospheric profiles (tropical, midlatitude, sub-arctic) and water vapor content. T_b sensitivities to D_{eff}, optical thickness, and IWP were much lower for atmospheres with high water vapor content. Due to this, accurate retrievals of cloud properties from ground-based observations requires the knowledge of atmospheric water vapor content and profile (Dubuisson et al. 2008).

Wang et al. (2011) developed a Fast IR Radiative Transfer Model that uses the 8.5 μm, 11 μm, and 12 μm bands to infer ice cloud optical thickness and D_{eff} from satellite-based IR measurements. A sensitivity study was conducted using the model for an ice cloud layer located between 8 km and 8.5 km under a tropical atmosphere in order to evaluate the feasibility of inferring optical thickness and D_{eff}. This was done by creating optical thickness and D_{eff} isolines corresponding to each ice cloud case from the split-window technique combined with a single window (11 μm and 12 μm). This revealed high sensitivity to small particle sizes (D_{eff} < 80 μm) as indicated by the wide separation of D_{eff} isolines based on the split-window technique. The retrieval of optical thickness is more accurate if only 11 μm or 12 μm T_bs are involved. It can be seen from the compression of the optical thickness and D_{eff} isolines that attempting to infer both optical thickness and D_{eff} from very optically thin (< 0.3) or optically thick (> 5) ice clouds will be extremely difficult and rife with uncertainties. The model was also used to simulate a single-layer cirrus cloud case that occurred on February 11, 2008. Surface, atmospheric profiles, and cloud geometry were obtained from Aqua Moderate Resolution Imaging Spectroradiometer (MODIS) collection-5, Cloud-Aerosol Lidar with Orthogonal Polarization (CALIOP), and Modern Era Retrospective-Analysis for Research and Applications (MERRA). Comparison between MODIS-retrieved and model-retrieved optical thickness and D_{eff} were made. It was found that MODIS-retrieved optical thicknesses tended to be larger than model-retrieved values while MODIS-retrieved D_{eff}s had more deviations from model-retrieved values in terms of magnitude. Despite this, since the absorption is dominate for ice clouds in the IR region, the model retrievals were less sensitive to particle habit distribution and vertical structure. This implied that model retrieval gave more reliable ice cloud properties than MODIS collection-5 products for optically thin ice cloud with small particles (Wang et al. 2011).

1.3. Theoretical Concerns

What can be observed for the reviewed studies focused on the inference of ice clouds using bands in the mm/sub-mm (microwave) region are that only simplified (i.e. single-habit ice clouds) polarized simulations have been conducted, few mm/sub-mm bands have been studied, and/or low frequency (high mm/sub-mm) bands have been studied. Idealized ice cloud cases such as clouds containing a single ice particle habit might be simple to perform or computationally efficient but it could underestimate or overestimate the usefulness of the mm/sub-mm bands. Despite this, it has been implied that using moderate to high frequency bands (> 150 GHz) could be useful for inferring ice cloud properties, especially cirrus clouds. Therefore, polarized simulations using realistic ice clouds (e.g. multiple ice habits and realistic cloud geometry) utilizing an ample amount of mm/sub-mm bands of relatively high frequency will be conducted for this study in order to evaluate their usefulness of inferring ice cloud properties.

It has been shown that using the IR bands within 8 μm – 13 μm atmospheric window along with the split-window technique can be beneficial for observing relatively thin ice clouds and inferring their properties such as optical thickness, IWP, and D_{eff}. It is possible that using polarized IR observations could also retrieve ice cloud properties though not many studies currently exist that provide a detailed background on the topic. With the addition of using polarized IR observations, they could possibly also be utilized with the split-window technique. Therefore, polarized simulations also utilizing the IR atmospheric window bands, particularly the 8.6 μm, 10.6 μm, and 12 μm bands, will be conducted for this study.

1.4. Outline of Study

Mm/sub-mm and LWIR wavelengths that were selected for this study were evaluated for their feasibility to infer IWP and D_{eff} by utilizing radiative transfer data calculated by ARTS. The data calculated by the ARTS simulator were first used in a series of sensitivity analyses involving the rate of change of brightness temperature with respect to D_{eff} at a given IWP for each mm/sub-mm and LWIR wavelength. Information gleaned from the analyses were then used to create 2D IWP and D_{eff} isoline LUTs involving 2 to 3 wavelengths with the goal of LUTs being useful for retrieving a broad range of IWPs and D_{eff}s. 3 ice particle habit mixtures were used: MODIS Collection-6 (MC6), Improved General Habit Model (IGHM), and the Two Habit Model (THM). This was done in order to evaluate what affects to the sensitivity analyses and LUTs would arise from using different habit mixture with the primary focus being on MC6. Retrievals of IWPs and D_{eff}s were then performed utilizing the MC6 LUTs through the use of radiances calculated from simulated realistic ice clouds generated by a program called Cloudgen. An error analysis of the retrieval was then conducted in order to evaluate the accuracies of the LUTs. The sensitivity analyses, LUTs, and retrievals were used as determining factors of how useful the mm/sub-mm and LWIR wavelengths will be for inferring ice cloud properties.

2. ATMOSPHERIC RADIATIVE TRANSFER SIMULATOR (ARTS) AND CLOUDGEN DESCRIPTION

The simulations done for this study were conducted by a fully polarized forward model known as the Atmospheric Radiative Transfer Simulator (ARTS) version 2. The ARTS simulator can perform simulations for 1D, 2D, and 3D atmospheres and allows users to modify various atmospheric parameters such as temperature and pressure levels specific to their situation. For this study, 1D simulations were carried out (Figure 1). The simulated atmosphere is represented as a 3D user-specified grid. The 1D scenario ignores the x- (longitude) and y-axis (latitude) of the atmospheric grid and only takes into account the z-axis (height).

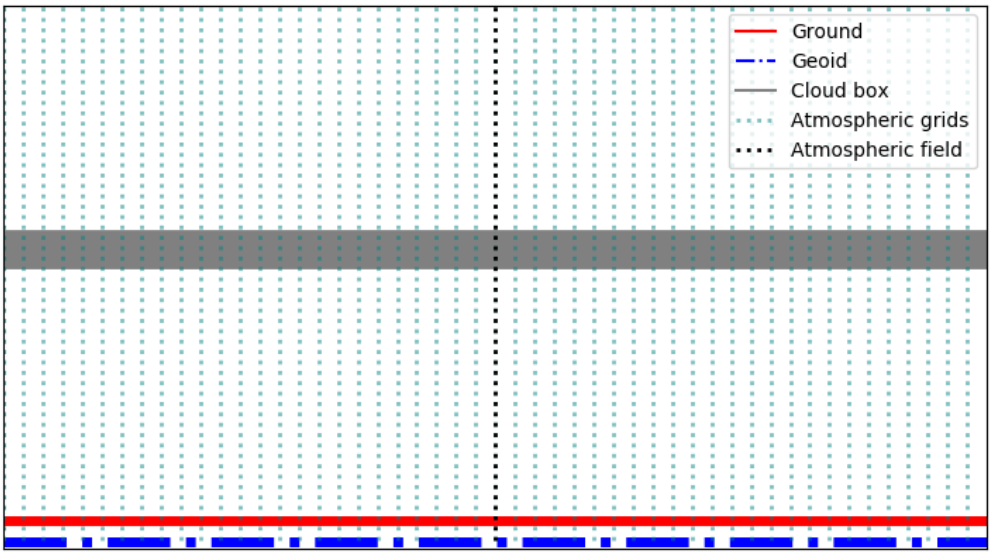

Figure 1. Schematic of a 1D atmosphere implemented in ARTS. The radius of the geoid, the surface and all pressure levels are constant around the globe. The extension of the cloud box is either from the surface up to a pressure level, or between two pressure levels (shown in the figure). The surface (ground) must be above the lowermost pressure level. Image adapted from Buehler et al. 2017.

ARTS's representation of the radiative transfer equation is described according to:

$$\frac{d\boldsymbol{I}}{ds}(\boldsymbol{n},\nu,T) = -\langle \boldsymbol{K}(\boldsymbol{n},\nu,T)\rangle \boldsymbol{I}(\boldsymbol{n},\nu,T) + \langle \boldsymbol{a}(\boldsymbol{n},\nu,T)\rangle B(\nu,T) + \int_{4\pi} d\boldsymbol{n}' \langle \boldsymbol{Z}(\boldsymbol{n},\boldsymbol{n}',\nu,T)\rangle \boldsymbol{I}(\boldsymbol{n}',\nu,T) \quad (1)$$

where $\boldsymbol{I}$ is the Stokes vector, $\langle \boldsymbol{K} \rangle$ is the ensemble-averaged extinction matrix, $\langle \boldsymbol{a} \rangle$ is the ensemble-averaged absorption vector, B is the Planck function, and $\langle \boldsymbol{Z} \rangle$ is the ensemble-averaged phase matrix. Furthermore, ν is the frequency of the radiation, T is the temperature, ds is a path-length element of the propagation path, and **n** is the propagation direction (Emde et al. 2004). The Planck function and Stokes vector will be discussed later in this study. This vector radiative transfer equation is for a medium with thermal emission including randomly distributed and oriented ice particles (Mishchenko et al. 2002). ARTS allows for the simple insertion of a cloud box into user-defined pressure levels of the simulated atmosphere (Figure 1) consisting of the single scattering properties of one to several particle types from inputted data files. ARTS solves the vector radiative transfer equation using two different methods: the backward Monte Carlo method and Discrete Ordinate Iterative (DOIT) method. The DOIT method, which was used for this study, solves the radiative transfer equation by restricting the scattering portion of the equation to be done only inside the cloud box in order to reduce computation time and memory (Emde et al. 2004).

2.1. ARTS Simulated Sensor Settings

Users can also change the settings of the simulated sensor such as setting its altitude and viewing zenith angle or modify it to match the specifications of existing radiometric

instruments. For the mm/sub-mm wavelength cases of 440.87 μm (680 GHz), 707.06 μm (424 GHz), 922.44 μm (325 GHz), 1362.69 μm (220 GHz), and 1638.21 μm (183 GHz) the sensor settings corresponding to the ICIR (IceCube Cloud-Ice Radiometer) instrument were used. ICIR is an 874 GHz radiometer primarily used to simultaneously retrieve IWP and D_{eff} (D. L. Wu et al. 2014). The sensor for the mm/sub-mm cases will have an altitude of 410 km (roughly ICIR height) and viewing zenith angle of 53.5°.

For the IR wavelength cases of 8.6 μm, 10.6 μm, and 12 μm the sensor settings corresponding to the MODIS instrument will be used. MODIS is an instrument that provides radiometric observations in 36 spectral bands ranging in wavelength from 0.4 μm to 14.4 μm at $\pm 55°$ scanning angles and at a 705 km height. The sensor for the IR cases will have an altitude of 705 km (MODIS height) and viewing zenith angles $\pm 55°$ from nadir (0°).

2.2. ARTS Simulated Cloud Box Settings and Cloudgen

2.2.1. Ice Cloud Layer for the Sensitivity Analyses and LUTs

For the sensitivity analyses and LUT creation, the cloud box was chosen to be at a pressure below 440 hPa with the layer being between 11 km and 13 km in altitude which corresponds to high altitude cirrus clouds (Feofilov et al. 2015). The thickness of the ice cloud for the simulations was determined to be 2 km thick in order to conform to observing optically thin ice clouds. Each ice cloud case were organized to have a certain IWP and D_{eff} value. The values of IWPs that were used for the simulations were: 10-200 gm^{-2} (increments of 10 gm^{-2}), 200-300 gm^{-2} (increments of 25 gm^{-2}), and 300-750 gm^{-2} (increments of 50 gm^{-2}). This range of IWPs was inspired by studies revealing that 75% of all high altitude ice clouds had IWPs smaller than 100 gm^{-2} (Feofilov et al. 2015). The values of D_{eff} that were used were: 10-200 μm (increments of 10 μm), 200-300 μm (increments of 20 μm), and 300-400 μm (increments of 25

μm). This range of D_{eff}s are values that would be typically found in cirrus clouds (Fauchez et al. 2015; Liu and Curry et al. 2000). The reason why the maximum values of IWPs and D_{eff}s are relatively high is to cover all possible cases of ice clouds and not just narrow the focus to thin cirrus.

2.2.2. Cloudgen

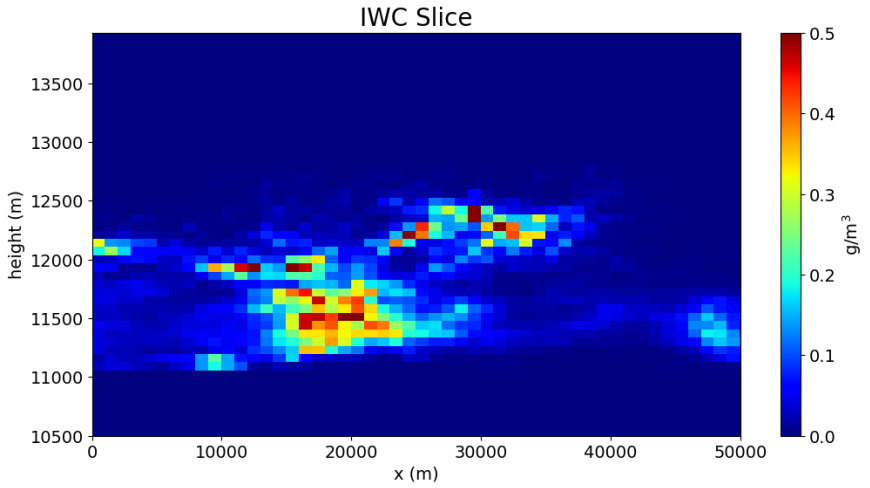

Figure 2. Example 2D slice of stochastic cirrus clouds represented as IWC (gm^{-3}) outputted by Cloudgen.

In order for retrievals to be conducted, observational data must be provided for comparison against the simulated data. Given the amount of wavelengths that was selected for this study, the attempt to find observational data provided by radiometric/polarimetric instruments that coincided to a particular location and time was going to be extremely difficult with numerous assumptions having to be made due to data collocation and absolving different resolutions between instruments. Instead, a program called Cloudgen was used to create synthetic – but heterogeneous – 3D ice clouds which can be inputted into ARTS. This is done by creating an input file for the Cloudgen program that lists the structural properties unique to ice clouds: fallstreak geometry, wind-shear induced mixing, and lognormally distributed ice water

contents (IWCs) and D_{eff}s (Hogan and Kew, 2005). The generated clouds are commonly outputted as IWCs (Figure 2) and D_{eff}s in an x-, y-, and z-axis coordinate system format in meters. IWCs can be integrated vertically to calculate IWPs. This means known values of IWP and D_{eff} can be calculated for error analyses of the retrieved results. The Cloudgen software package also includes example files for idealized stratocumulus and cirrus clouds. This study utilized the idealized cirrus cloud with variable D_{eff} and a series of 1 km by 1 km pixel 1D simulations corresponding to each separate pixel of the outputted 3D ice cloud was conducted and will be described in more detail in the retrieval section of this thesis.

2.3. ARTS Simulated Atmosphere Settings

The pressure and the temperature levels used for the simulated atmosphere for the 1D scenarios were provided by the ARTS software package and website and corresponds to what is found the typical tropical atmosphere (Figure 3).

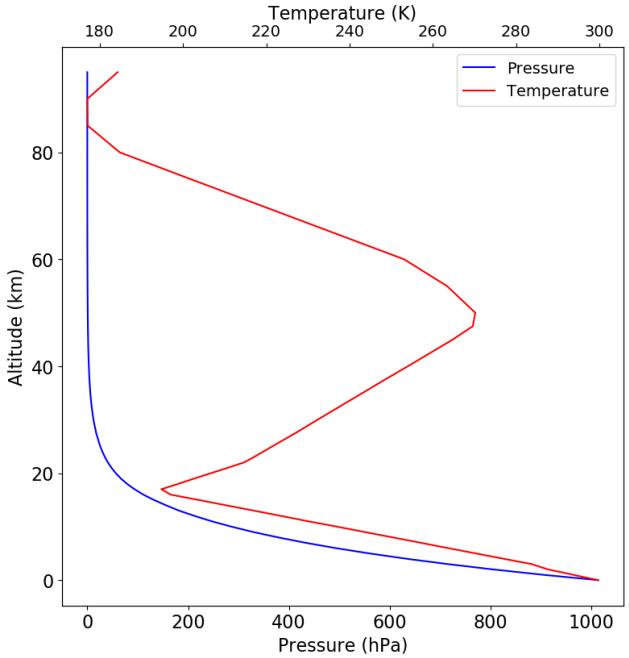

Figure 3. Pressure (bottom x-axis) and temperature (top x-axis) profiles used by ARTS to simulate an atmosphere similar to what is typically observed in a tropical atmosphere.

3. THE ICE CLOUD MODEL

Radiative transfer simulators such as ARTS requires a cloud property input(s) along with the definition of the location of the cloud(s). For ice clouds, properties are generated through the definition of an ice particle size distribution and particle shape (habit) mixture that can involve only 1 particle habit to even more than 5. The purpose of these ice cloud parameters are to provide a realistic representation of the ice cloud to the simulator and are useful when comparisons are made with in situ observations. This section discusses the ice particle property sources, ice particle size distribution, and habit mixtures that were used as input for the ARTS simulator.

3.1. Ice Particle Properties Database

Ice particle single scattering properties for the mm/sub-mm scenarios will also be provided by Yang et al. (2013). The same amount of properties and habits that are available for the IR wavelengths are also available in the mm/sub-mm region. However, 4 separate temperature scenarios (160 K, 200 K, 230 K, and 270 K) are available due to the discovery that the single-scattering properties of ice particles are noticeably temperature dependent at mid-IR and larger wavelengths (Iwabuchi and Yang, 2011). Fortunately, ARTS allows for the cloud box to be composed of ice particles under different given temperatures. ARTS would then interpolate the temperatures within the cloud box according to the user-defined altitude resolution and atmospheric profiles.

Ice particle single scattering properties for the IR scenarios will be provided by Yang et al. (2013). The particle properties will consist of wavelength, maximum particle dimension (ranging from 2 μm to 10000 μm), particle volume, projected area, extinction efficiency, single-

scattering albedo, and asymmetry factor. 3 degrees of particle surface roughness are also available: smooth, moderately rough, and extremely rough. Moderately rough and severely rough ice particles will be used for this study. A total of 16 habits are available from the database: hexagonal 10-plate aggregate, hexagonal 5-plate aggregate, hexagonal 8-column aggregate, droxtal, hollow bullet rosette, solid bullet rosette, single solid hexagonal column, single hollow hexagonal column, single hexagonal plate, sphere, oblate spheroid (aspect ratio: 1.25, 2.5, 4.0), and prolate spheroid (aspect ratio: 0.25, 0.5, 0.75).

3.2. Ice Particle Size Distribution: D_{eff}, IWP, and Particle Number Density Calculation

3.2.1. The Gamma Size Distribution

The ice particles that the simulated cloud boxes were comprised of was under a gamma size distribution which has been commonly used represent realistic ice clouds (e.g. J. Miao et al. 2003; Dubuisson et al. 2008). The gamma distribution equation is as follows:

$$N(D) = N_0 D^{\mu} e^{-\lambda D} \tag{2}$$

where D is the maximum dimension of an ice crystal particle, $N(D)$ is the number density of the ice crystal particles corresponding to D, N_0 is the intercept, μ is the dispersion, and λ is the slope. The slope, λ, is broken down as follows:

$$\lambda = \frac{\mu + 3}{D_{eff}} \tag{3}$$

where μ is the dispersion and D_{eff} is the effective diameter.

3.2.2. D_{eff} Calculation

Solving the gamma distribution described in Eq. (2) will yield the bulk properties of the ice cloud, including D_{eff}, which can be defined as:

$$D_{eff} = \frac{3}{2}\frac{\int_{D_{min}}^{D_{max}}[\sum_{i=1}^{N} f_i(D)V_i(D)]\,N(D)\mathrm{d}D}{\int_{D_{min}}^{D_{max}}[\sum_{i=1}^{N} f_i(D)A_i(D)]\,N(D)\mathrm{d}D} \tag{4}$$

where D_{min} and D_{max} are the minimum and maximum sizes of D in the given particle size distribution $N(D)$, N is the number of particle habits within the distribution, i denotes the ice particle habit, $f_i(D)$ is the ice particle habit fraction for habit i at a D, $V_i(D)$ and $A_i(D)$ is the volume and average projected area of the habit i for a given D. With the use of the habit fraction, $f_i(D)$, one can use original or existing habit mixtures as part of the calculation of the gamma distribution.

3.2.3. Particle Number Density Calculation

Bulk (mean) volume ($\bar{V}$) can also be calculated from the size distribution and is defined as follows:

$$\bar{V} = \frac{\int_{D_{min}}^{D_{max}}[\sum_{i=1}^{N} f_i(D)V_i(D)]\,N(D)dD}{\int_{D_{min}}^{D_{max}}[\sum_{i=1}^{N} f_i(D)]\,N(D)dD} \tag{5}$$

where all parameters retain the same definition as described in Eq. (4). Using $\bar{V}$ and given the ice water path (IWP) of the ice cloud will allow the calculation of the particle number density which

can be then used as input representing the ice cloud for the ARTS simulator. The IWP is defined as follows:

$$IWP = \int_{z_1}^{z_2} IWC \, dz \tag{6}$$

where IWC is the ice water content at a particular altitude (z), z_1 is the ice cloud base altitude, and z_2 is the ice cloud top altitude. It should be noted that for the $53.5°$ scenarios the true IWP of the slant viewing angle can be obtained by dividing Eq. (6) by the cosine of the viewing angle:

$$IWP_\theta = \frac{IWP}{\cos\theta} \tag{7}$$

where θ is the viewing angle. For the sake of consistency, all IWPs regardless of viewing angle in this study are calculated from the nadir viewing position ($\theta = 0°$). In general, IWPs at the $53.5°$ viewing angle are 59.4% greater than nadir IWPs. IWC can be obtained from Eq. (6) by rearranging the equation to solve for IWC in order to calculate particle number density. IWC is defined as follows:

$$IWC = \frac{IWP}{z_2 - z_1} \tag{8}$$

where IWP is divided by the ice cloud thickness represented as the difference between the ice cloud top altitude (z_1) and base altitude (z_2). This is making the assumption that IWC is constant for all heights covered by the ice cloud. The calculated IWC can then be used to calculate the

particle number density (n_p) for all heights of the ice cloud. The n_p calculation is defined as follows:

$$n_p = \frac{IWC}{\rho_i \overline{V}} \tag{9}$$

where ρ_i is density of ice (931 kg/m^3) and $\overline{V}$ is bulk particle volume. n_p can then be inputted into ARTS to represent the ice cloud. As described before, Cloudgen outputs ice clouds as IWC in an x-, y-, and z-axis coordinate system format which can be used to directly calculate n_p to represent the inhomogeneous ice cloud for retrievals.

3.3. Ice Particle Habit Mixtures

For this study 3 ice particle habit mixtures were used in the ARTS simulator: MODIS Collection-6 (MC6), Improved General Habit Mixture (IGHM), and Two-Habit Model (THM). This subsection describes the ice particle habits that comprise these mixtures.

3.3.1. MODIS Collection-6 (MC6)

The MC6 habit mixture is composed of only severely roughed hexagonal 8-column aggregates under a gamma distribution (Platnick et al. 2015). The reason that severely roughened particles are used for this mixture rather than the idealized, perfectly smooth particles are to better represent natural ice particles.

3.3.2. Improved General Habit Mixture (IGHM)

The IGHM (Baum et al. 2011) consists of a total of 9 habits: droxtal, hollow and solid bullet rosette, hollow and solid hexagonal column, single hexagonal plate, hexagonal 8-column aggregate, hexagonal 5-plate aggregate, and hexagonal 10-plate aggregate. The percentage of particle habits changes linearly as size changes (Figure 4).

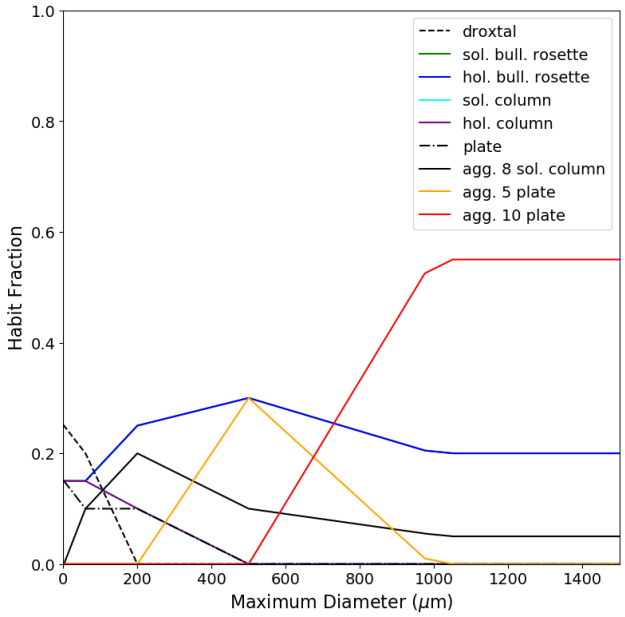

Figure 4. IGHM consisting of 9 ice particle habits with fractions changing linearly as size changes. It can be seen the aggregates mainly populate large particle sizes. Reprinted from Baum et al. 2011. © **American Meteorological Society. Used with permission.**

The IGHM is considered to be an improvement to the original MODIS Collection-5 habit mixture which defined discrete habit fractions for certain ranges of sizes. The habit fraction as shown in Figure 4 can be inputted into $f_i(D)$ in order to calculate ice particle bulk properties that conform to the IGHM.

3.3.3. Two-Habit Model (THM)

A THM had been developed by Liu et al. (2014) that included a single hexagonal column and a hexagonal 20-column aggregate. This was due to the fact that in situ observations noted that ice particles are generally separated into simple and complex categories with the complex category generally dominating in larger particle sizes (Schmitt and Heymsfield, 2014). The equations that govern the THM with the single column habit fraction (f_c) function are shown in Eq. (10). The hexagonal 20-column aggregate habit fraction can be simply obtained by

subtracting f_c from 1. The use of the THM had shown to be in close agreement with in situ measurements from 11 field campaigns (Liu et al. 2014). For this study, the hexagonal 8-column aggregate will replace the 20-column aggregate as the representative "complex" particle in the THM due to it being available for both IR and mm/sub-mm regions (Figure 5).

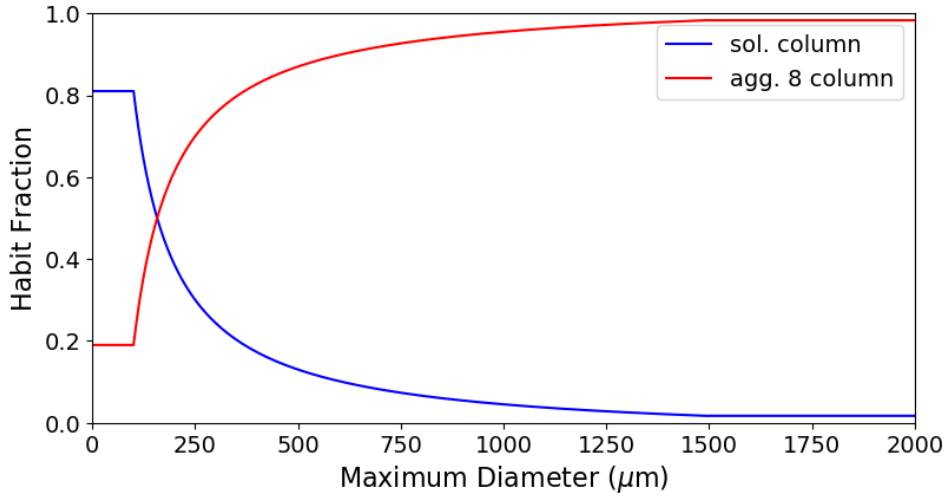

Figure 5. The THM used by Liu et al. 2014 with ice particle habit fraction as a function of particle size. It can be seen that the hexagonal 8-column aggregate (agg. 8 sol. column) eventually dominates the habit mixture as particle size increases. Image adapted from Liu et al. 2014.

$$f_c(D) = \begin{cases} 0.81 & D < 100\mu m \\ \dfrac{85}{D} - 0.04 & 100\mu m \leq D < 1500\mu m \\ 0.017 & D \geq 1500\mu m \end{cases} \quad (10)$$

4. BRIGHTNESS TEMPERATURE PARAMETERS AND LUT METHODOLOGY

The radiances calculated from the ARTS simulations are in $Wm^{-2}Hz^{-1}sr^{-1}$. Being a fully polarized model, ARTS can output radiances for all 4 components of the Stokes vector though the user can have the simulator output less components to save computation time. The components of the Stokes vector are defined as follows:

$$\boldsymbol{I} = [I, Q, U, V] \tag{11}$$

where I is the full intensity of the radiation, Q is the difference between vertical and horizontal polarization, U is the difference for $\pm 45°$ polarization, and V is the difference between left and right circular polarization. The first 2 components of the Stokes vector – I and Q – were the components that were considered for this study.

The outputted radiances can be then converted into T_b using the Planck function. The Planck function with respect to incident frequency (υ) and radiance (I) is defined as follows:

$$T_b(\nu, I) = \frac{h\nu}{\log\left(\frac{2h\nu^3}{Ic^2} + 1\right)k} \tag{12}$$

where $h = 6.626 \times 10^{-34}$ J s is Planck's constant, $c = 2.998 \times 10^{8}$ m s^{-2} is the speed of light, and $k = 1.381 \times 10^{-23}$ J/K is Boltzmann's constant. The T_bs could then be used to create useful parameters for inferring ice cloud properties. For this study, the LWIR split-window technique

(BTD), the mm/sub-mm brightness temperature depression relative to clear-sky (ΔT_b), and the polarization difference (PD) were the parameters that were utilized for the sensitivity analyses and the creation of the LUTs for the retrievals. This section briefly discusses how the brightness temperature parameters are calculated.

4.1. LWIR Split-Window Technique (BTD)

The split-window technique (BTD) is the difference between the T_bs of a "clean" window IR band (little absorption of water vapor) (e.g. 8.6 μm) and a "dirty" window (moderate absorption of water vapor) (e.g. 10.6 μm and 12 μm). The split-window technique is primarily used for cloud classification with BTD > 0 K indicating the presence of ice clouds and BTD < 0 K indicating the presence of volcanic/aerosol clouds. As discussed in the literature review, using the BTD parameter is expected to be highly sensitive to optically thin cirrus clouds (low IWP and D_{eff}). For this study, the BTDs that will be used will be 8.6 μm – 10.6 μm, and 8.6 μm – 12 μm.

4.2. Mm/sub-mm Brightness Temperature Relative to Clear-Sky (ΔT_b)

The brightness temperature relative to clear-sky (ΔT_b) calculation is as follows:

$$\Delta T_b = T_{bclearsky} - T_b \tag{13}$$

where ΔT_b is calculated by subtracting brightness temperature observed in a cloudy scenario (T_b) from brightness temperature observed in a clear-sky scenario ($T_{bclearsky}$). As discussed in the literature review, ice particle size affects the IWP-ΔT_b relation significantly and since the particle size effects on ΔT_b depend on microwave frequency, the ratio of ΔT_bs at two adjacent frequencies may contain particle size information (Evans and Stephens, 1995b; Liu and Curry,

2000). With the use of low mm/sub-mm wavelengths (high frequency microwave bands), the ΔT_b parameter can be expected to be highly sensitive to optically thin ice clouds and thus easily infer their properties.

4.3. Polarization Difference (PD)

The Polarization Difference (PD) calculation is as follows:

$$T_{bv} = T_b(I + Q) \tag{14.1}$$

$$T_{bh} = T_b(I - Q) \tag{14.2}$$

$$PD = T_{bv} - T_{bh} \tag{14.3}$$

where T_{bv} (Eq. 14.1) is calculated by taking the sum of the I and Q components of the Stokes vector and then calculating the T_b of the result through the use of Eq. (12), T_{bh} (Eq. 14.2) is calculated by taking the difference between the I component of the Stokes vector and the Q component of the Stokes vector and then calculating the T_b of the result. PD can be then calculated by taking the difference between T_{bv} and T_{bh} Eq. (14.3). The PD parameter has been commonly used to represent polarized observations (e.g. J. Miao et al. 2003; Davis et al. 2007) and have been found to be sensitive to particle size and habit. Because of this, it was expected that PDs of the habit mixtures used in this study would have the greatest differences in PDs.

4.4. IWP and D_{eff} Isoline LUT Methodology

The 2D IWP and D_{eff} isoline LUTs that were created for this study uses the brightness temperature parameters for different wavelengths for the x- and y-axes. The cirrus cloud cases calculated in ARTS are plotted in a way to create lines of constant IWPs and D_{eff}s (isolines) with each intercept representing a specific cirrus cloud case (Figure 6). The degree of separation between the IWP or D_{eff} isolines will be the indicator of how sensitive the wavelengths are to

changes in IWP and D_{eff}. A large separation between the isolines will indicate a high IWP and D_{eff} sensitivity while compressed isolines will indicate little or negligible sensitivity. If the wavelengths representing both axes of the LUT are sensitive to a fairly large range of IWP and D_{eff}, then the LUT will likely result in the appearance of evenly distributed isolines across the plot almost similar to a square/rectangle grid. This will indicate that it will be easier to simultaneously retrieve IWP and D_{eff} using the wavelengths and brightness temperature parameters selected for the plot.

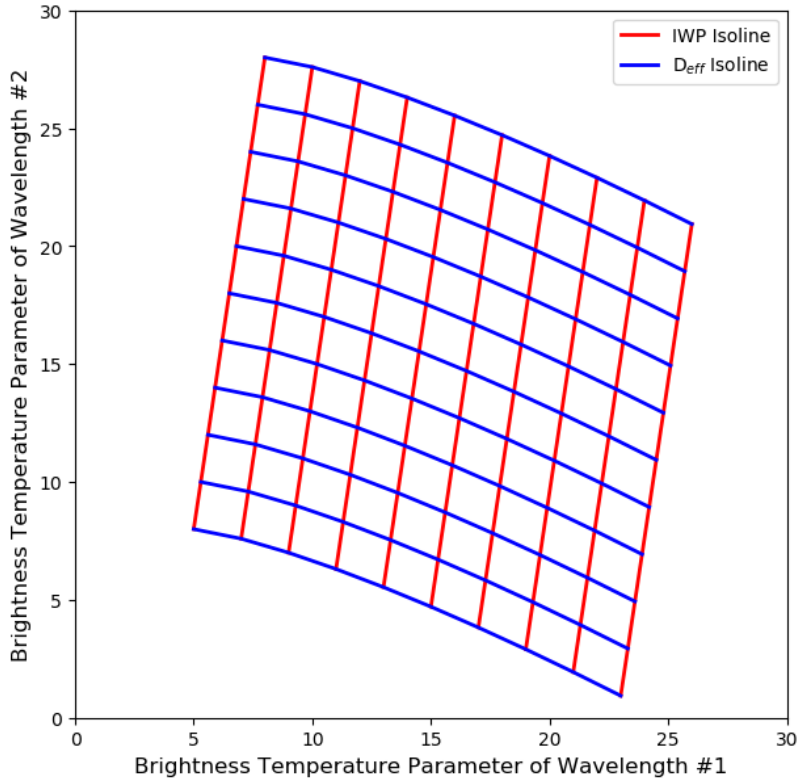

Figure 6. An example 2D IWP and D_{eff} isoline LUT. The LUT should typically exhibit a grid-like format where IWP and D_{eff} isolines are organized by descending/ascending values. The isolines are plotted with respect to corresponding brightness temperature parameters (BTD/ΔT_b/PD) of 2 or more wavelengths.

Cubic spline interpolation was conducted for the 2D LUTs retrievals in order to account for the presence of curved isolines that might be present. A cubic spline is a spline constructed of piecewise third-order polynomials that pass through a set of n control points. A single third-order polynomial is defined as:

$$Y_i(t) = a_i + b_i t + c_i t^2 + d_i t^3 \tag{15}$$

where t is a parameter $t \in [0,1]$ and $i = 0, \dots, n-1$. The second derivative of each polynomial is set to zero at the endpoints which provides a boundary condition that completes the system of $n-2$ equations. This produces a square matrix representing the coefficients of the system of equations with nonzero elements only on the diagonal and slots horizontally or vertically adjacent to the diagonal (tridiagonal matrix). The system of equations could then be solved easily to give the coefficients of the polynomials (Weisstein et al. 2019). The 2D LUTs that were used for retrievals were inputted into a Python program that utilizes a module called SciPy (Scientific Python) that has a function called "interp2d" for interpolation over a 2D grid that allowed for cubic spline interpolation. After the interpolation was conducted, a nearest-neighbor approximation was used to determine a corresponding IWP and D_{eff} from a given pair of brightness temperature parameters. The error analyses of the retrievals were represented as the percentage error which is defined as:

$$Percentage\ Error = \frac{|x_{est} - x_{obs}|}{x_{obs}} \tag{16}$$

where x_{est} is the estimated value and x_{obs} is the observed/measured value. The absolute value of the difference between the estimated and observed value is initially taken and then divided by the observed value in order to obtain the mean percentage error of the IWP and D_{eff} retrievals.

5. RESULTS

5.1. Sensitivity Analyses and LUTs Discussion

5.1.1. LWIR Split-Window BTD Sensitivity Analysis

Both the 8.6 μm – 10.6 μm and 8.6 μm – 12 μm split-window BTDs exhibited similar sensitivities to IWP and D_{eff} at both viewing angles. The 53.5° viewing angle MC6 BTD rates of change (Figures 7A and 8A) show sharp decreases in BTD ($\delta BTD/\delta D_{eff}$ < -2.5 K/μm) primarily concentrated at very low values of IWP (< 50 gm^{-2}) and D_{eff} (< 50 μm) indicating high sensitivity to low values of D_{eff}. The rates of change rapidly approaches to 0 K/μm as D_{eff} increases (D_{eff} > 50 μm) meaning that BTD stagnates regardless IWP and D_{eff} indicating insensitivity to moderate and high values of D_{eff}. For 8.6 μm – 10.6 μm, the increase in IWP (> 50 gm^{-2}) does slightly lower the BTD rate of change due to the decrease in BTD magnitude with the lowest values of D_{eff} (< 50 μm) containing BTDs decreasing from a maximum of about 5 K for IWPs > 100 gm^{-2} (Figure 7D). For 8.6 μm – 12 μm, the increase of IWP significantly lowers BTD also due to the decrease of BTD magnitude with the lowest values of D_{eff} containing BTDs decreasing from a maximum of about 10 K for IWPs > 100 gm^{-2} (Figure 8D).

MC6 and THM (Figures 7C and 8C) are in close agreement with each other for all values of IWPs and D_{eff} despite solid columns dominating the THM for low D_{eff}s. The overall IGHM BTD rates of change (Figure 7B and 8B) are somewhat similar to the other habit mixtures, however, the IGHM has the most disagreement with a general overestimation of BTD that can be observed clearly in the BTD vs. D_{eff} line plots of Figures 7D and 8D.

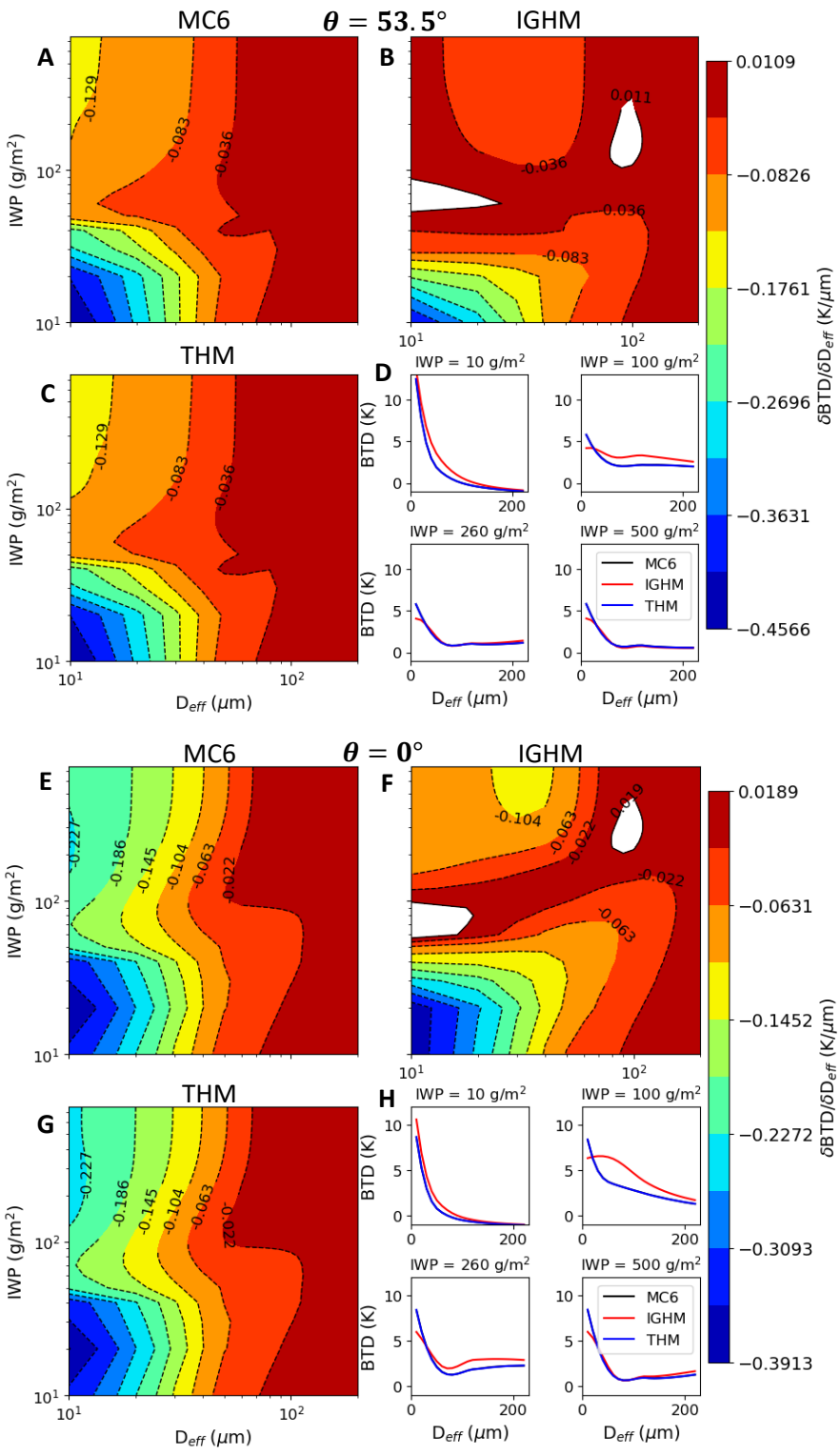

Figure 7. Contour and line plot sets representing sensitivities of 8.6 μm – 10.6 μm BTDs with respect to IWP and D_{eff} at 53.5° and 0° (nadir) viewing angles. (A, E), (B, F), and (C, G) are contour plots displaying $\delta BTD/\delta D_{eff}$ for MC6, IGHM, and THM. (D, H) are D_{eff} vs. BTD plots for IWPs of 10 gm^{-2}, 100 gm^{-2}, 260 gm^{-2}, and 500 gm^{-2}.

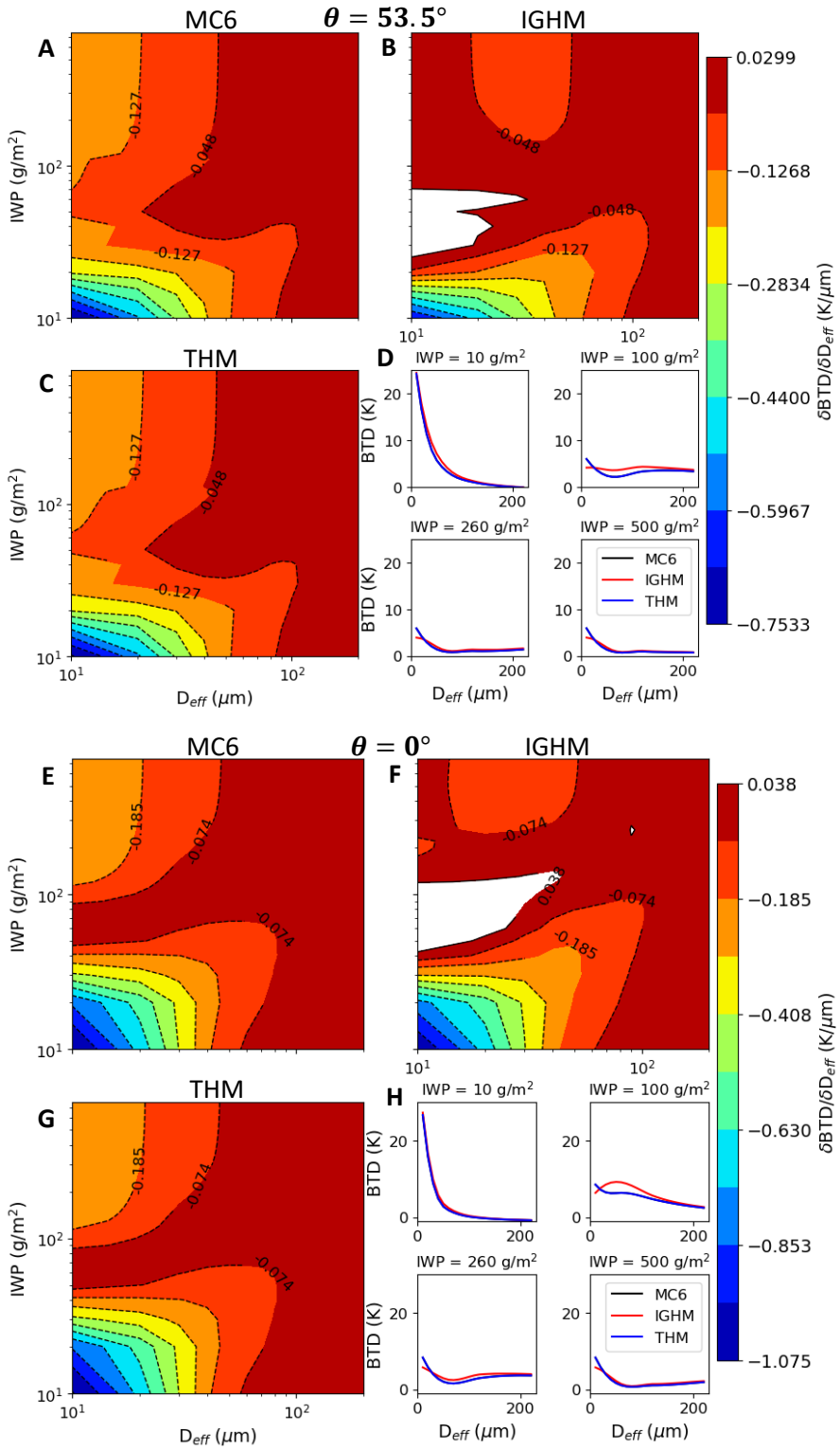

Figure 8. Contour and line plot sets representing sensitivities of 8.6 μm – 12 μm BTDs with respect to IWP and D_{eff} at 53.5° and 0° (nadir) viewing angles. (A, E), (B, F), and (C, G) are contour plots displaying $\delta BTD/\delta D_{eff}$ for MC6, IGHM, and THM. (D, H) are D_{eff} vs. BTD plots for IWPs of 10 gm^{-2}, 100 gm^{-2}, 260 gm^{-2}, and 500 gm^{-2}.

With the incorporation of several more particle habits into the IGHM compared to MC6 and THM it appears to have a noticeable effect on split-window BTD meaning it will likely affect the how LUTs would be constructed and retrievals.

The nadir viewing angle MC6 BTD rates of change (Figures 7E and 8E) are relatively similar to what was observed at 53.5° with sharp decreases in BTDs ($\delta BTD/\delta D_{eff}$ < -2.5 K/μm) when IWP < 50 gm^{-2} and D_{eff}< 50 μm indicating high sensitivity and rapid stagnation of BTDs for greater IWPs and D_{eff} indicating insensitivity. The magnitudes of the BTDs are greater at nadir due to the IWPs of the incident radiation being less than the actual IWP along the 53.5° viewing angle resulting in greater attenuation of 12 μm T_bs and thus an increase in the split-window BTD. The IGHM still generally overestimates BTDs (Figures 7F and 8F) while the THM remains in close agreement with MC6 (Figures 7G and 8G).

5.1.2. LWIR Split-Window BTD LUTs

Using the information gleaned from the split-window BTD sensitivity analysis, a set of 12 μm T_bs vs. 8.6 μm – 12 μm BTDs LUTs were created and used for retrievals (53.5° viewing angle only). At the 53.5° viewing angle (Figure 9A), the greatest IWP and D_{eff} isoline separation for cloud cases with IWP < 70 gm^{-2} and D_{eff} < 50 μm. This is due to the high BTD sensitivity to low values of IWP and D_{eff}. The isolines rapidly compress for higher values of IWP and D_{eff} due to insensitivity which will complicate retrievals and will likely be a primary source of error. Figure 9B shows that there is high IGHM deviation from MC6 (< 1.5) for low to moderate IWPs (10 gm^{-2} < IWP < 100 gm^{-2}) and D_{eff}s (20 μm < D_{eff} < 100 μm). This means that if a LUT was to be created from the IGHM, then it would be noticeably different from MC6 and thus it would have an effect on retrievals.

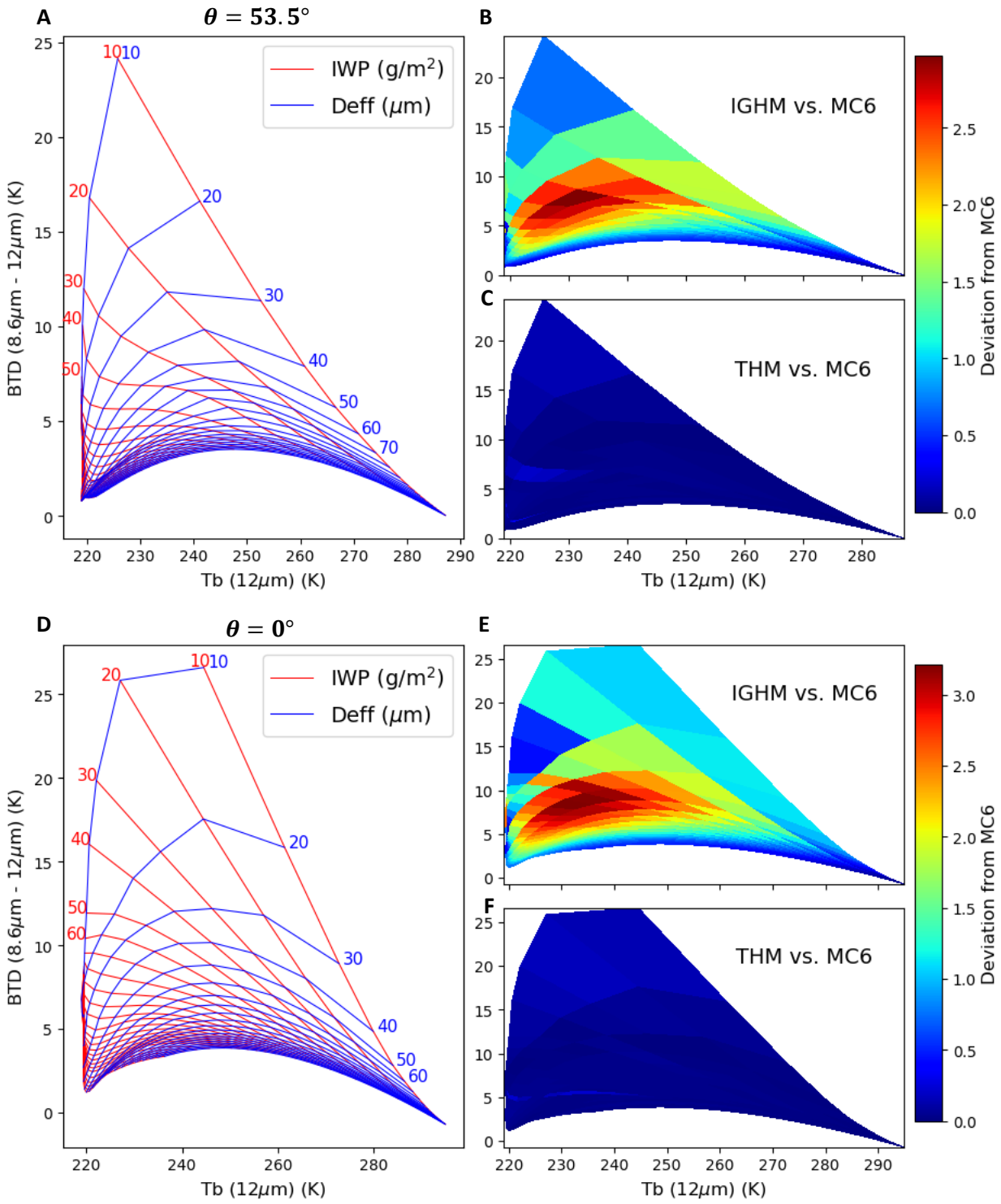

Figure 9. (A, D) MC6 IWP (red lines) and D_{eff} (blue lines) isoline LUT plots of 8.6 µm – 12 µm BTDs with respect to 12 µm T_bs at 53.5° and 0° (nadir) viewing angles. (B, E) contour plot of IGHM unit deviation from MC6 fitted in between the LUT isolines of (A, D). (C, F) contour plot of IGHM unit deviation from MC6 fitted in between the LUT isolines of (A, D).

The THM (Figure 9C) is in relatively in good agreement (deviation from MC6 < 0.5) with MC6 meaning that a THM LUT would be similar to the MC6 LUT and have little effect on retrievals. The nadir MC6 LUT (Figure 9D) has similar isoline structure to the $53.5°$ scenario with great separation for low IWPs and D_{eff}s and rapid isoline compression for higher IWPs and D_{eff}s. The IGHM deviation from MC6 is still greatest for low to moderate IWPs and D_{eff}s while the THM remains in good agreement with MC6.

5.1.3. Mm/sub-mm ΔT_b Sensitivity Analysis

At 183 GHz (1636 μm) the highest MC6 ΔT_b sensitivities ($\delta\Delta T_b/\delta D_{eff}$ > 0.1 K/μm) are within moderate and large values of IWPs (> 200 gm^{-2}) and D_{eff}s (100 μm < D_{eff} < 400 μm) for both viewing angles (Figures 10A and 10E). As D_{eff} increases from 200 μm, $\delta\Delta T_b/\delta D_{eff}$ begins to decrease meaning the rate of ΔT_b increase is slowing down and thus ΔT_b sensitivity decreases. The IGHM ΔT_b rates of change are generally less in magnitude than MC6 (Figure 10B and 10F) leading to an underestimation of ΔT_bs which can also be observed in Figures 10D and 10H particularly for IWPs > 200 gm^{-2} and D_{eff}s > 250 μm. Despite this, the IGHM ΔT_bs are still sensitive to moderate and large values of IWPs and D_{eff}s. The THM is in very close agreement with MC6 due to the ΔT_b rates of change having nearly the same magnitudes (Figures 10C and 10G) and can also be observed by the overlapping THM (blue) and MC6 (black) lines for all values of IWPs and D_{eff}s (Figure 10D and 10H).

At 220 GHz (1363 μm) the highest MC6 ΔT_b sensitivities ($\delta\Delta T_b/\delta D_{eff}$ > 0.1 K/μm) shift to slightly lower values of D_{eff} (70 μm < D_{eff} < 350 μm) while remaining highly sensitive to moderate and large values of IWPs (> 200 gm^{-2}) for both viewing angles (Figures 11A and 11E). As D_{eff} increases from 200 μm, $\delta\Delta T_b/\delta D_{eff}$ begins to decrease resulting in decreasing ΔT_b sensitivity.

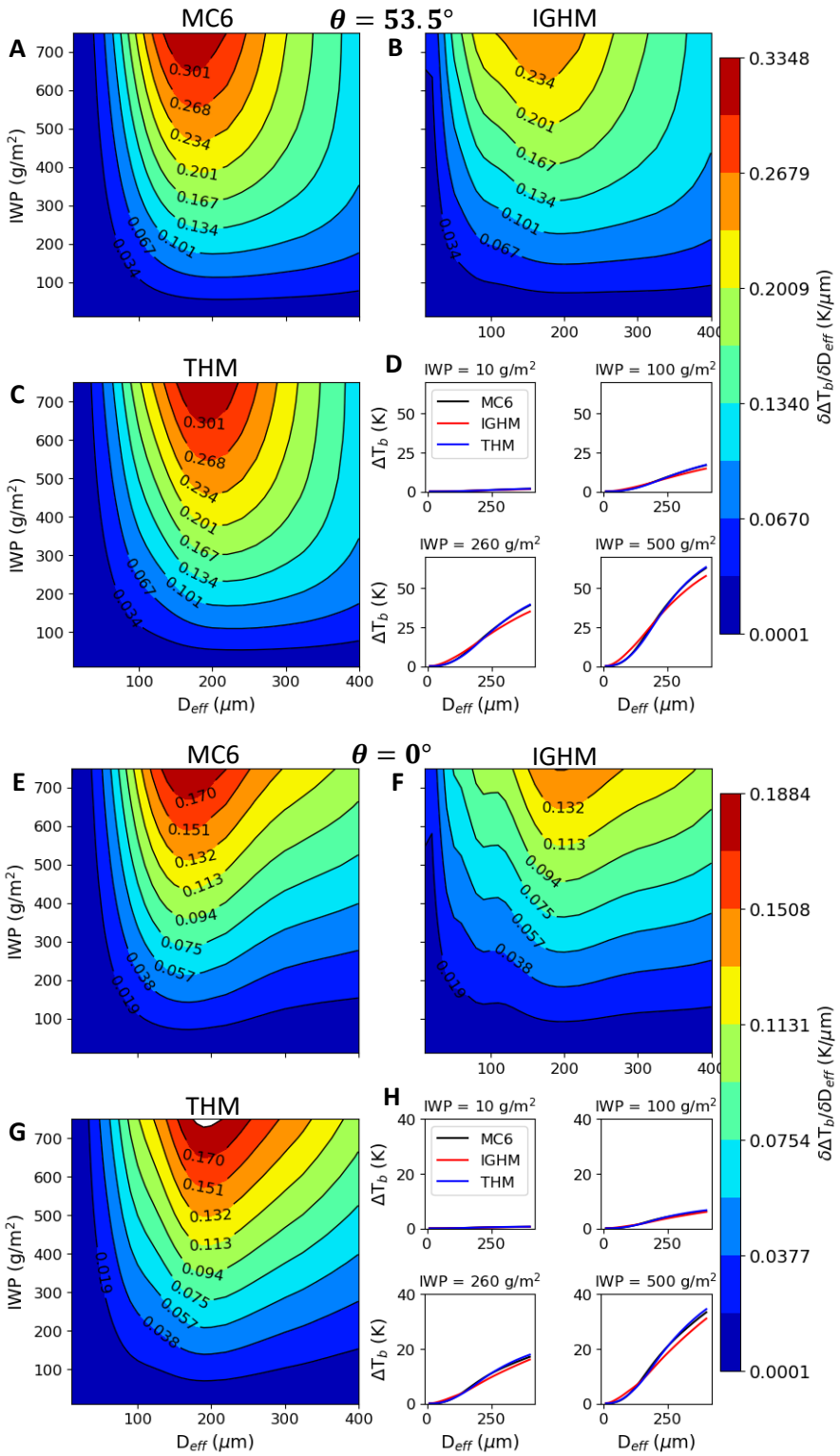

Figure 10. Contour and line plot sets representing sensitivities of 183 GHz (1636 μm) ΔT_bs with respect to IWP and D_{eff} at 53.5° and 0° (nadir) viewing angles. (A, E), (B, F), and (C, G) are contour plots displaying $\delta\Delta T_b/\delta D_{eff}$ for MC6, IGHM, and THM. (D, H) are D_{eff} vs. ΔT_b plots for IWPs of 10 gm^{-2}, 100 gm^{-2}, 260 gm^{-2}, and 500 gm^{-2}.

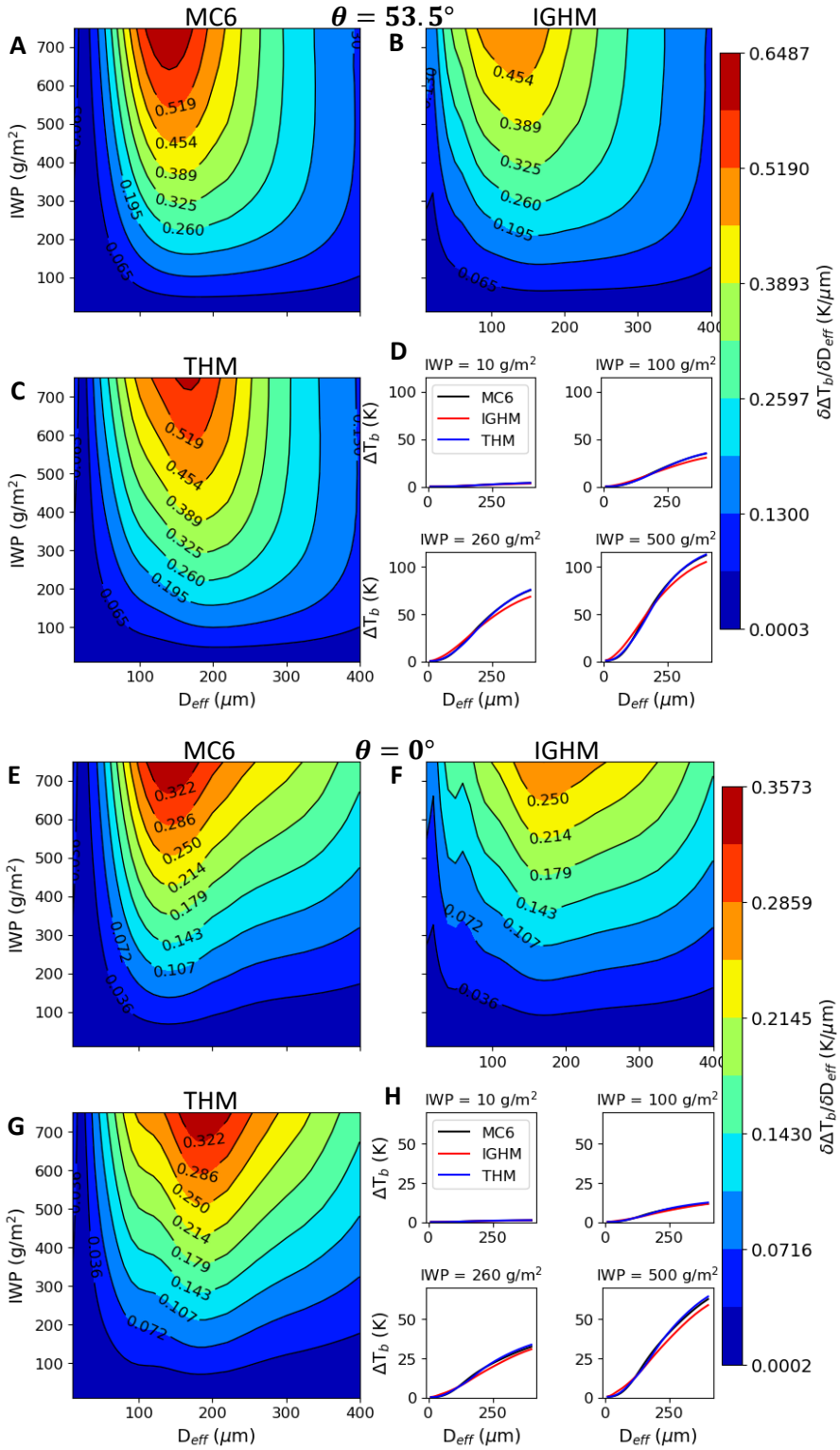

Figure 11. Contour and line plot sets representing sensitivities of 220 GHz (1363 μm) ΔT_bs with respect to IWP and D_{eff} at 53.5° and 0° (nadir) viewing angles. (A, E), (B, F), and (C, G) are contour plots displaying $\delta\Delta T_b/\delta D_{eff}$ for MC6, IGHM, and THM. (D, H) are D_{eff} vs. ΔT_b plots for IWPs of 10 gm^{-2}, 100 gm^{-2}, 260 gm^{-2}, and 500 gm^{-2}.

The IGHM ΔT_b rates of change still generally underestimates ΔT_b compared to MC6 (Figures 11B and 11F) which can also be observed in Figures 11D and 11H particularly for IWPs > 200 gm^{-2} and D_{eff}s > 250 μm. The THM is still in very close agreement with MC6 (Figure 11C, 11D, 11G, and 11H). The overall range of ΔT_bs covered by the ice cloud cases are greater than what was observed at 183 GHz, reaching ΔT_bs as high as 100 K at $53.5°$ (Figure 11D) and as high as 60 K at nadir (Figure 11H). This is due to 183 GHz being a water vapor profiling frequency meaning it is primarily sensitive to altitudes generally below where ice clouds, especially cirrus, are typically located resulting in lower ΔT_bs being observed than the higher frequencies.

At 325 GHz (922 μm) the highest MC6 ΔT_b sensitivities ($\delta \Delta T_b / \delta D_{eff}$ > 0.1 K/μm) shift to even lower values of D_{eff} (50 μm < D_{eff} < 200 μm) than 183 GHz and 220 GHz while remaining highly sensitive to moderate and large values of IWPs (> 200 gm^{-2}) for both viewing angles (Figures 12A and 12E). As D_{eff} increases from 250 μm, $\delta \Delta T_b / \delta D_{eff}$ begins to decrease to near 0 K/μm resulting in the stagnation of ΔT_b which can clearly be observed in Figures 12D and 12H. This indicates that 325 GHz ΔT_bs are insensitive to large D_{eff}s. The lower IGHM ΔT_b rates of change still generally underestimates ΔT_b compared to MC6 (Figures 12B and 12F) which can also be observed in Figures 12D and 12H particularly for IWPs > 200 gm^{-2} and D_{eff}s > 200 μm. The THM actually begins to overestimate ΔT_b compared to MC6 for the same range of IWPs and D_{eff}s due to the higher rates of change (Figures 122C and 12G).

At 680 GHz (441 μm) the highest MC6 ΔT_b sensitivities ($\delta \Delta T_b / \delta D_{eff}$ > 0.1 K/μm) shift to even lower values of D_{eff} (10 μm < D_{eff} < 200 μm) than the lower frequencies. There is also a noticeable shift in high ΔT_b sensitivities to lower IWPs (> 100 gm^{-2}) for both viewing angles (Figures 13A and 13D).

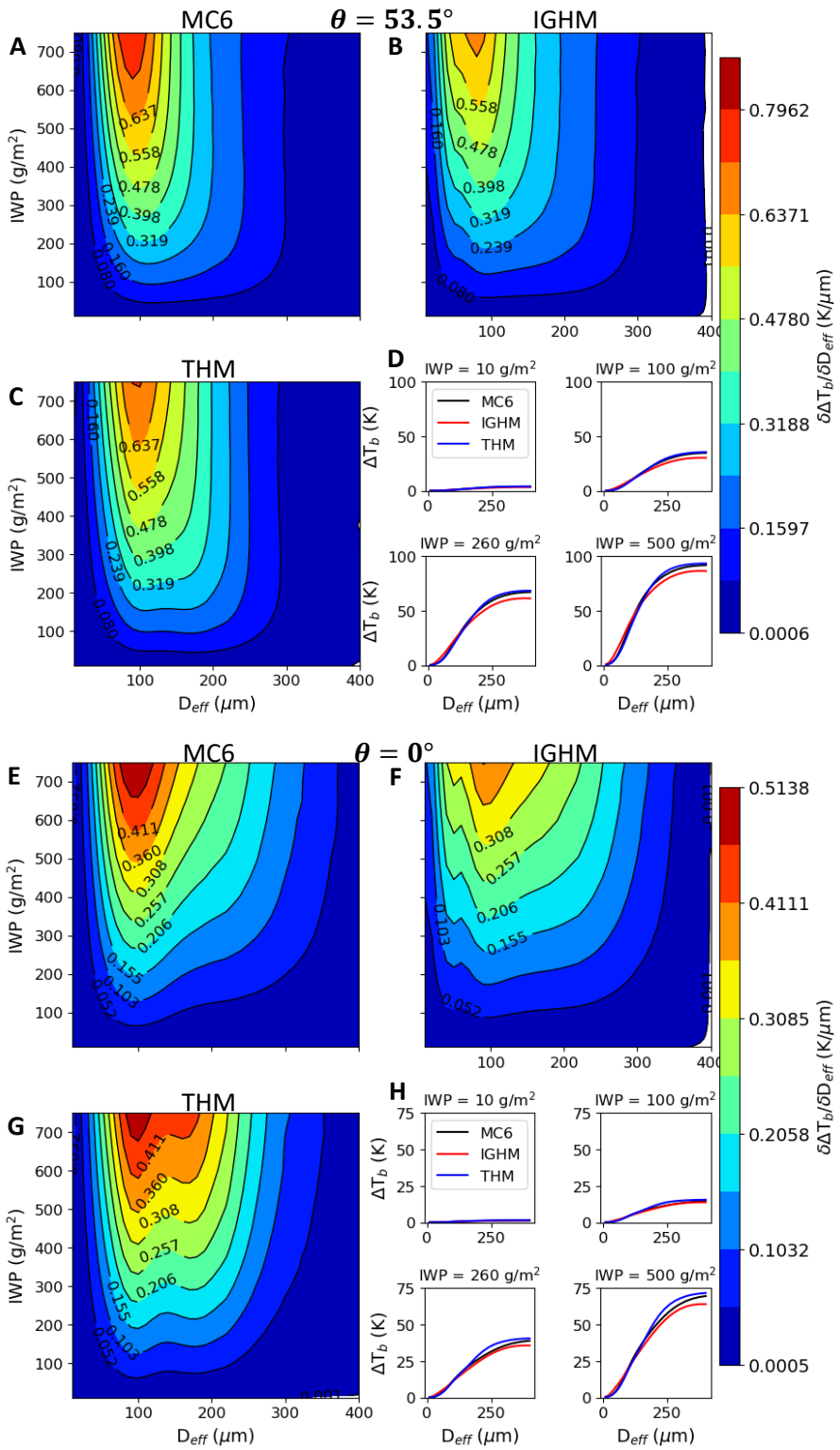

Figure 12. Contour and line plot sets representing sensitivities of 325 GHz (922 μm) ΔT_bs with respect to IWP and D_{eff} at 53.5° and 0° (nadir) viewing angles. (A, E), (B, F), and (C, G) are contour plots displaying $\delta\Delta T_b/\delta D_{eff}$ for MC6, IGHM, and THM. (D, H) are D_{eff} vs. ΔT_b plots for IWPs of 10 gm^{-2}, 100 gm^{-2}, 260 gm^{-2}, and 500 gm^{-2}.

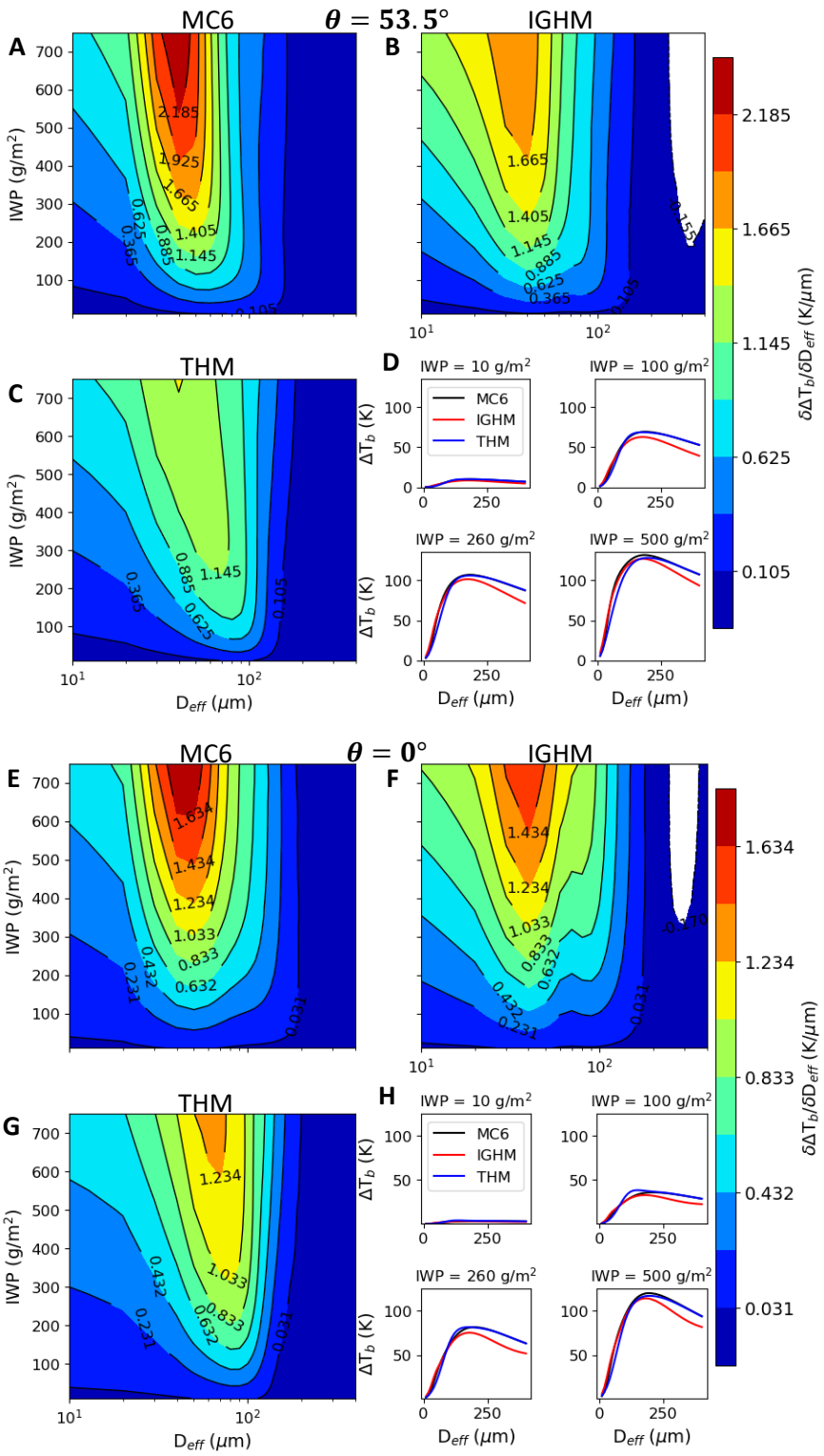

Figure 13. Contour and line plot sets representing sensitivities of 680 GHz (441 μm) ΔT_bs with respect to IWP and D_{eff} at 53.5° and 0° (nadir) viewing angles. (A, E), (B, F), and (C, G) are contour plots displaying $\delta\Delta T_b/\delta D_{eff}$ for MC6, IGHM, and THM. (D, H) are D_{eff} vs. ΔT_b plots for IWPs of 10 gm^{-2}, 100 gm^{-2}, 260 gm^{-2}, and 500 gm^{-2}.

As D_{eff} increases from 250 μm, $\delta\Delta T_b/\delta D_{eff}$ eventually approaches 0 K/μm and even becoming negative resulting in the stagnation and decrease in ΔT_bs for the largest D_{eff}s. This D_{eff} relationship can be observed clearly in Figures 13D and 13H. The decrease in ΔT_b could be due to the large D_{eff}s being similar in size as the 680 GHz (441 μm). This means that the scattering regime is approaching geometric optics where radiation exits the particles in different directions thus decreasing the amount of radiation scattered in the direction of incidence. The lower IGHM ΔT_b rates of change still underestimates ΔT_bs compared to MC6 (Figures 13B and 13F) which can also be observed in Figures 12D and 12H particularly for IWPs > 100 gm^{-2} and D_{eff}s > 200 μm. The lower THM ΔT_b rates of change (Figures 13C and 13G) also results in the underestimation of ΔT_bs particularly for low values of D_{eff}s (< 100 μm) and then approaches close agreement to MC6 for larger D_{eff}s.

5.1.4. Mm/sub-mm ΔT_b LUTs

The way that the sub-mm/mm ΔT_bs were utilized in the LUTs in this study were based on the ΔT_b ratio LUTs developed in the study done by Liu and Curry (2000). It was demonstrated that taking the ratio of adjacent frequencies could contain particle size information. This can be explained by the shift of high ΔT_b sensitivities to lower D_{eff}s as mm/sub-mm frequencies increases (wavelength decreases) that was discussed in the previous sub-section. The MC6 220 GHz/183 GHz ΔT_b ratio and 680 GHz ΔT_b LUTs (Figure 14A and 14D) were created in order to exploit the sensitivity that 680 GHz has toward relatively small ice particles, even more so than 325 GHz. At the 53.5° viewing angle (Figure 14A), there is a pronounced curve of the IWP and D_{eff} isolines for IWPs < 30 gm^{-2} and D_{eff}s < 60 μm. This is primarily due to the 183 GHz and 220 GHz having similar rates of change corresponding to those IWPs and D_{eff}s thus resulting in a stagnation of the ΔT_b ratio.

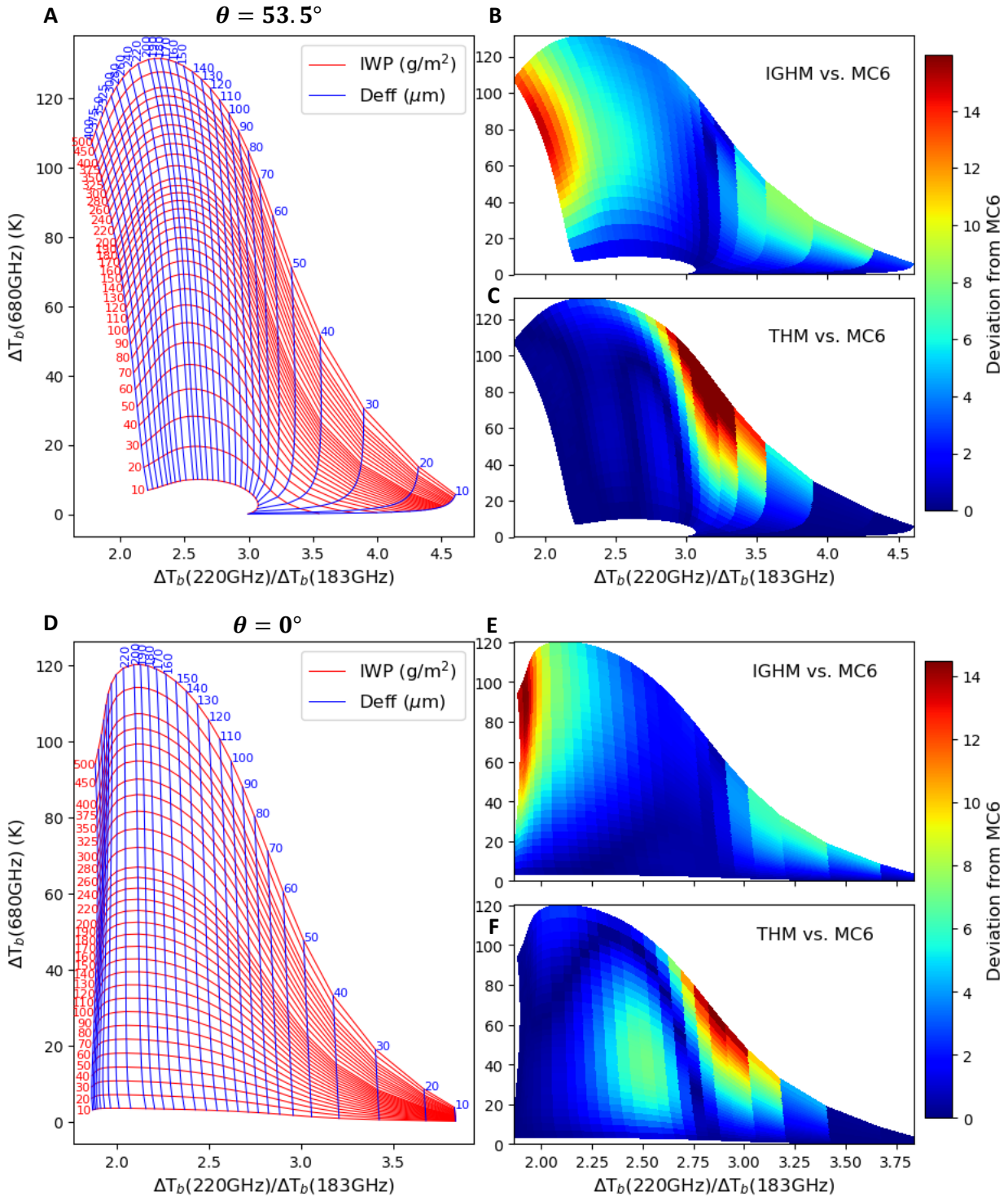

Figure 14. (A, D) MC6 IWP (red lines) and D_{eff} (blue lines) isoline LUT plots of 680 GHz ΔT_bs with respect to 220 GHz/183 GHz ΔT_b ratio at 53.5° and 0° (nadir) viewing angles. (B, E) contour plot of IGHM unit deviation from MC6 fitted in between the LUT isolines of (A, D). (C, F) contour plot of IGHM unit deviation from MC6 fitted in between the LUT isolines of (A, D).

The D_{eff} isolines curve downward towards lower 680 GHz ΔT_bs when D_{eff} > 200 μm as the scattering signature for relatively large ice particles decrease as discussed in the previous sub-section. There is decent separation of the IWP and D_{eff} isolines for primarily D_{eff}s > 100 μm and nearly all IWPs indicating the potential of accurate simultaneous retrievals. There is great separation of D_{eff} isolines but compressions of IWP isolines for D_{eff}s < 100 μm indicating the potential of accurate D_{eff} retrievals but inaccurate IWP retrievals. The IGHM deviation from MC6 is greatest for the largest values of IWPs (> 150 gm^{-2}) and D_{eff}s (> 240 μm) for both viewing angles (Figures 14B and 14E). The THM deviation from MC6 is greatest for the largest values of IWPs (> 200 gm^{-2}) and small to moderate values of D_{eff} (30 μm < D_{eff} < 150 μm) for both viewing angles (Figures 14C and 14F).

5.1.5. PD Sensitivity Analysis

The IR wavelengths of 8.6 μm (Figure 15A), 10.6 μm (Figure 15E), and 12 μm (Figure 15I) show a sharp increase of MC6 PD ($\delta PD/\delta D_{eff}$ > 0.01 K/μm) for low IWP and D_{eff} values (IWP < 100 gm^{-2}, D_{eff} < 100 μm) indicating high sensitivity. PDs eventually begin to stagnate to a certain maximum as D_{eff} increases. For 8.6 μm, PD stagnates to a maximum value of about 4 K at an IWP of 10 gm^{-2} as observed in Figure 15D. For 10.6 μm and 12 μm, PD stagnates to a maximum value of about 8 K at an IWP of 10 gm^{-2} as observed in Figures 15H and 15L. The IGHM and THM appear to completely agree with MC6 which can be seen in the appearance of a single line in the D_{eff} vs. PD line plots of Figures 15D, 15H, and 15L. Overall, 10.6 μm and 12 μm appear to be the most useful for IWP and D_{eff} retrieval due to the high sensitivity to low IWPs and D_{eff}s, the consistent increase of PD as D_{eff} increases, and the range of PDs covered by all cloud cases compared to 8.6 μm.

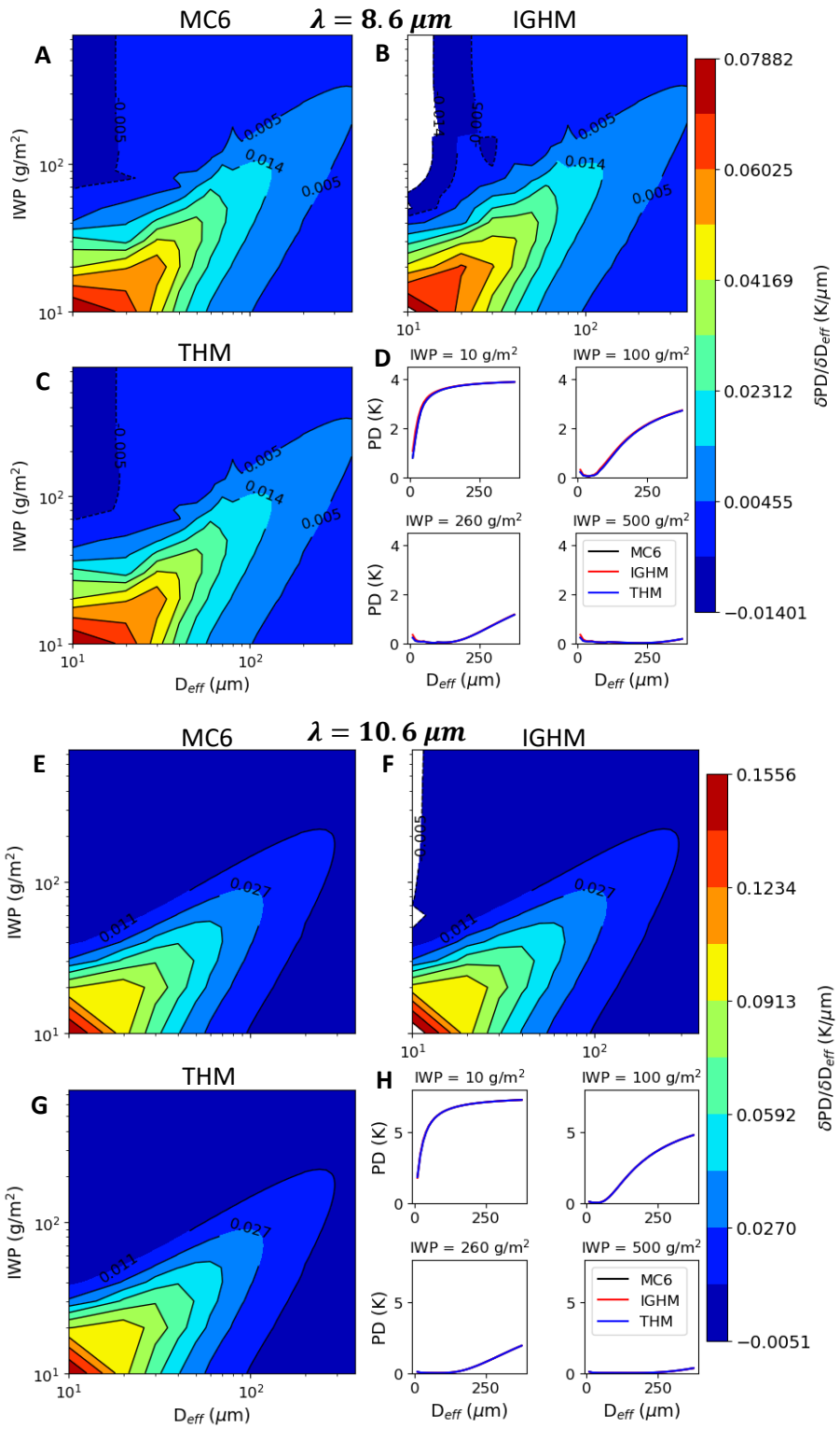

Figure 15. Contour and line plot sets representing sensitivities of 8.6 µm (A – D), 10.6 µm (E – H), and 12 µm (I – L) PDs with respect to IWP and D_{eff} at the 53.5° viewing angle. (A, E, I), (B, F, J), and (C, G, K) are contour plots displaying $\delta PD/\delta D_{eff}$ for MC6, IGHM, and THM. (D, H, L) are D_{eff} vs. PD plots for IWPs of 10 gm^{-2}, 100 gm^{-2}, 260 gm^{-2}, and 500 gm^{-2}.

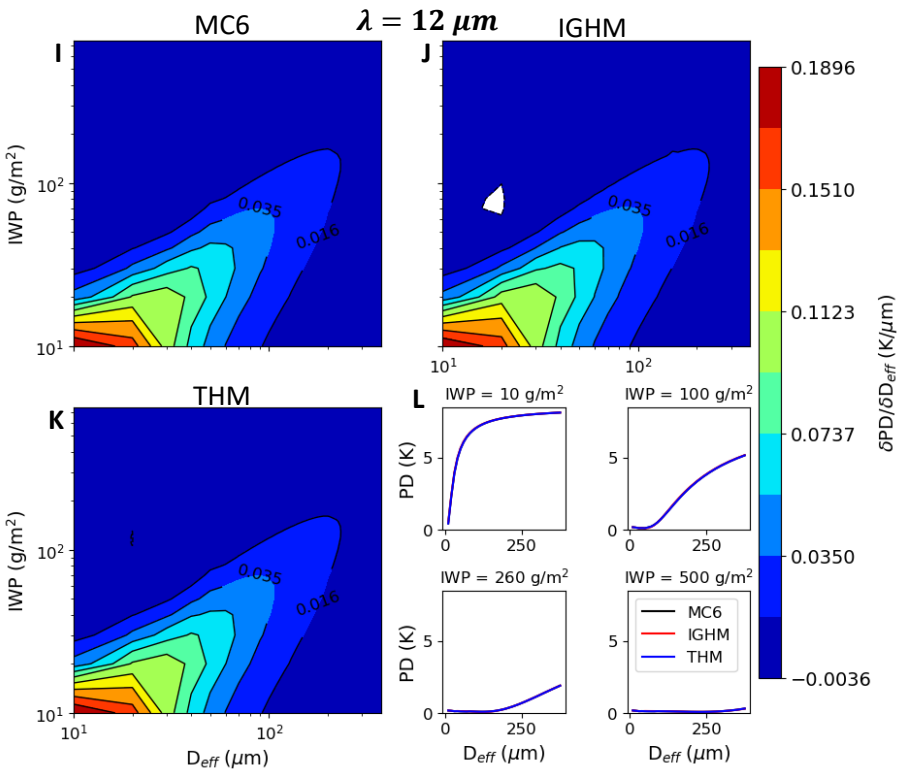

Figure 15. (Continued)

At 183 GHz (1636 µm), the positive PD rates of change ($\delta PD/\delta D_{eff}$ > 0.01 K/µm) indicates an initial sharp increase as D_{eff} increases for moderate values of D_{eff} (100 µm < D_{eff} < 200 µm) indicating high sensitivity (Figure 16A). PD then eventually reaches a maximum and then slightly decreases for large values of D_{eff} (> 250 µm) particularly for IWPs > 200 gm^{-2}. This relationship takes the form of a parabolic curve, which will be referred as a "resonance feature" as defined by J. Miao et al. (2003), which can be observed in the D_{eff} vs. PD plots (Figure 16D). The resonance feature poses as an obstacle for simultaneous IWP and D_{eff} retrievals due to likelihood of 2 or more D_{eff}s corresponding to the same PDs resulting in ambiguity. The resonance feature is more pronounced as IWP increases (IWP > 100 gm^{-2}) meaning that 183 GHz PDs are sensitive to large IWPs.

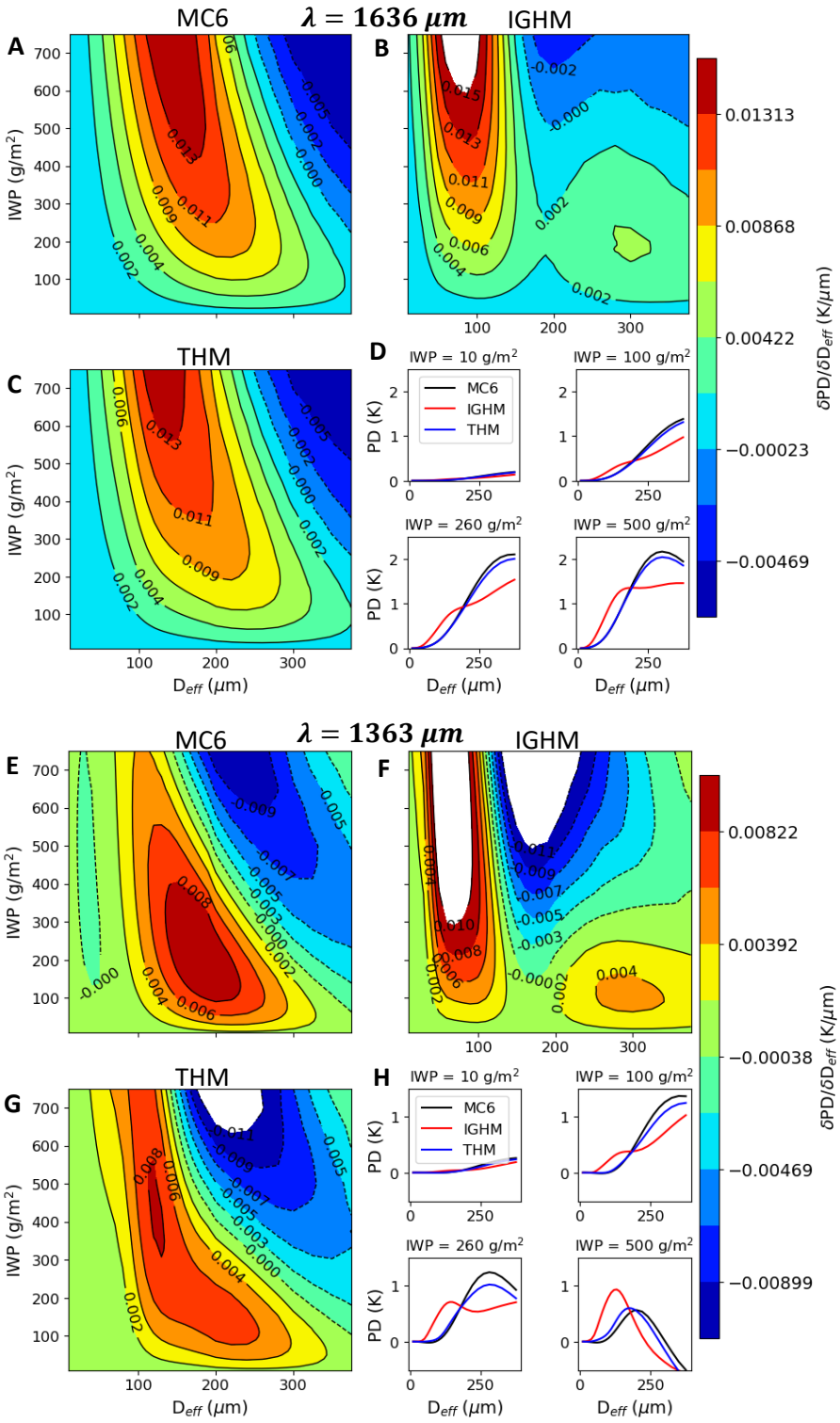

Figure 16. Contour and line plot sets representing sensitivities of 183 GHz (1636 μm) and 220 GHz (1363 μm) PDs with respect to IWP and D_{eff} at the 53.5° viewing angle. (A, E), (B, F), and (C, G) are contour plots displaying $\delta PD/\delta D_{eff}$ for MC6, IGHM, and THM. (D, H) are D_{eff} vs. ΔT_b plots for IWPs of 10 gm^{-2}, 100 gm^{-2}, 260 gm^{-2}, and 500 gm^{-2}.

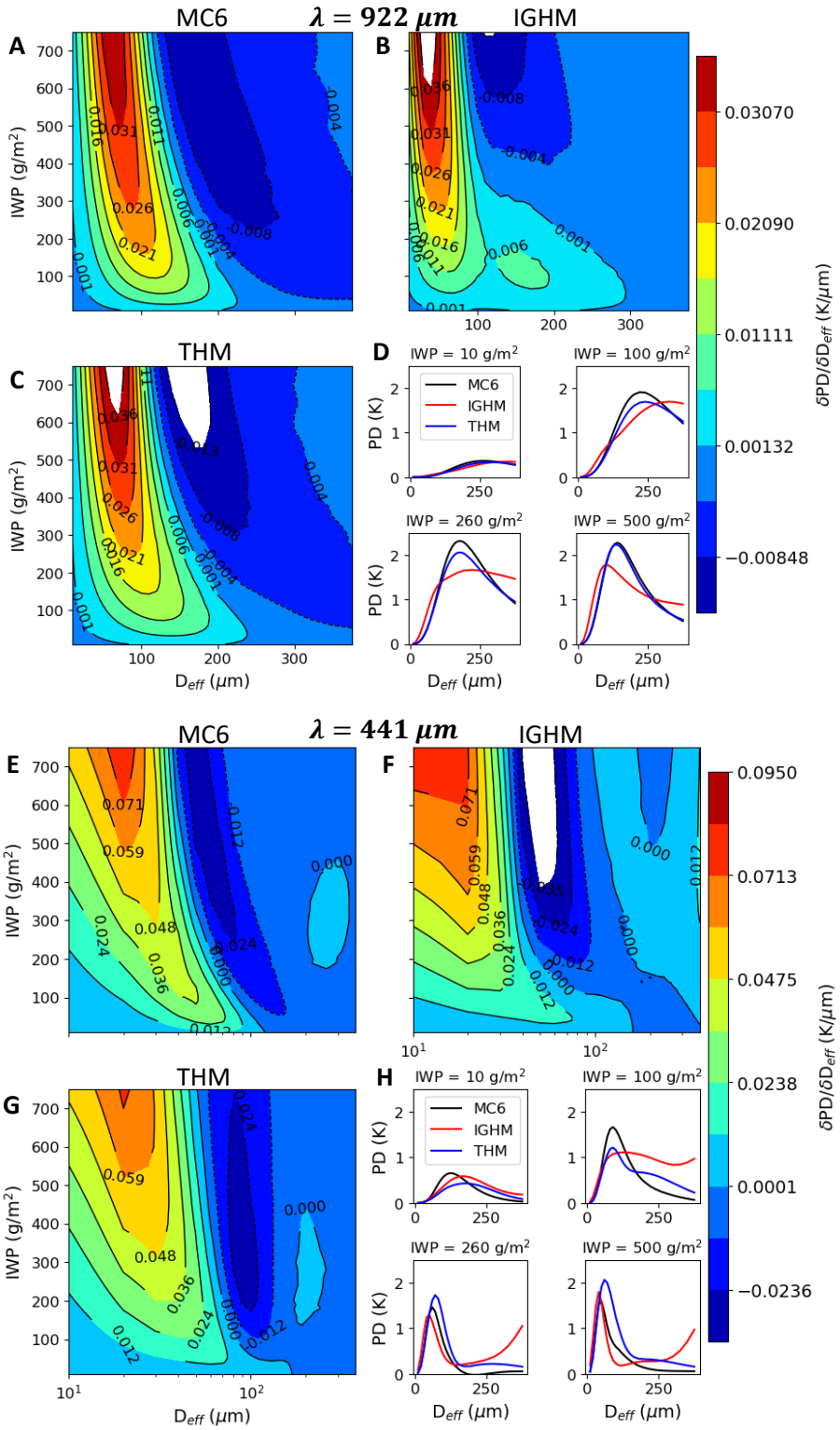

Figure 17. Contour and line plot sets representing sensitivities of 325 GHz (922 μm) and 680 GHz (441 μm) PDs with respect to IWP and D_{eff} at the 53.5° viewing angle. (A, E), (B, F), and (C, G) are contour plots displaying $\delta PD/\delta D_{eff}$ for MC6, IGHM, and THM. (D, H) are D_{eff} vs. ΔT_b plots for IWPs of 10 gm^{-2}, 100 gm^{-2}, 260 gm^{-2}, and 500 gm^{-2}.

The IGHM (Figure 16B) exhibits a complex D_{eff}-PD relationship resulting in an overestimation of PDs for D_{eff}s < 200 μm and then an underestimation of PDs for D_{eff}s > 200 μm compared to MC6 which can clearly be observed in Figure 16D. The THM has similar PD rates of change (Figure 16C) but when D_{eff} > 200 μm there is an underestimation in PDs compared to MC6 which can also be observed in Figure 16D.

At 220 GHz (1363 μm) the MC6 D_{eff}-PD relationship is similar to what was observed at 183 GHz: an initial increase in PD eventually reaching a maximum followed by a decrease in PD as D_{eff} increases resulting in the presence of the resonance feature (Figure 16E). There is, however, a slight shift in the resonance peak towards slightly lower values of D_{eff} indicating higher sensitivity to smaller ice particles compared to 183 GHz. The resonance feature is also more pronounced as IWP increases (> 100 gm^{-2}) meaning that 220 GHz PDs are sensitive to large IWPs. The IGHM (Figure 16F) also exhibits a complex D_{eff}-PD relationship resulting in an overestimation of PDs for D_{eff} < 200 μm and then an overestimation of PDs for D_{eff}s > 200 μm compared to MC6. The THM still has similar PD rates of change (Figure 16G) but when D_{eff} > 200 μm there is an underestimation in PDs compared to MC6.

At 325 GHz (922 μm), the MC6 resonance feature shifts to even lower D_{eff}s as observed by large, positive $\delta PD/\delta D_{eff}$s (> 0.02 K/μm) being concentrated at D_{eff}s between 50 μm and 100 μm and large, negative $\delta PD/\delta D_{eff}$s (< -0.01 K/μm) being concentrated at D_{eff}s between 150 μm and 200 μm (Figure 17A). This indicates that 325 GHz is more sensitive to smaller ice particles than the lower frequencies. The resonance feature is still more pronounced for large values of IWPs (> 100 gm^{-2}) indicating that 325 GHz is also sensitive to large IWPs. The IGHM has PDs rapidly increasing towards a maximum for smaller D_{eff}s (< 100 μm) than MC6 but at a smaller maximum PD (Figure 17B) leading to a general underestimation of values. The PDs then

begin to decrease at a slower rate than MC6 leading to an overestimation of values. The THM generally has an underestimation of PDs as clearly observed in Figure 17D and in the larger negative PD rates of change for large D_{eff}s (Figure 17C).

At 680 GHz (441 μm), the MC6 resonance feature shifts to even lower D_{eff}s than the lower frequencies. This is observed by large, positive $\delta PD/\delta D_{eff}$s (> 0.03 K/μm) being concentrated at D_{eff}s between 10 μm and 50 μm and large, negative $\delta PD/\delta D_{eff}$s (< -0.01 K/μm) being concentrated at D_{eff}s between 50 μm and 100 μm (Figure 17D). This indicates that 680 GHz is sensitive to the smallest ice particles than the lower frequencies. 680 GHz is also sensitive to large IWPs due to the increasing size of the resonance feature. The IGHM and THM has a general overestimation of PDs for moderate and large D_{eff}s which can be observed in Figure 17H.

5.1.6. PD LUTs

The 220 GHz vs. 183 GHz PD LUT (Figure 18A) was created due to both the frequencies providing a consistent increase in PD for most of the D_{eff}s used in this study which prevents folding of the isolines caused by the resonance feature. There is decent separation of the IWP and D_{eff} isolines for IWPs > 200 gm^{-2} and D_{eff}s > 150 μm while the isolines rapidly compress and converge to 0 K for smaller values of IWPs and D_{eff}s. This indicates that the 220 GHz and 183 GHz LUT will likely be useful for accurate simultaneous retrievals of moderate and large values of IWPs and D_{eff}s. The IGHM deviation from MC6 are greatest (> 0.6) for IWPs between 330 gm^{-2} and 500 gm^{-2} and D_{eff}s between 90 μm and 160 μm (Figure 18B). The THM deviation from MC6 are relatively low (< 0.2) compared to the IGHM indicating that the THM is in close agreement with the MC6 LUT (Figure 18C).

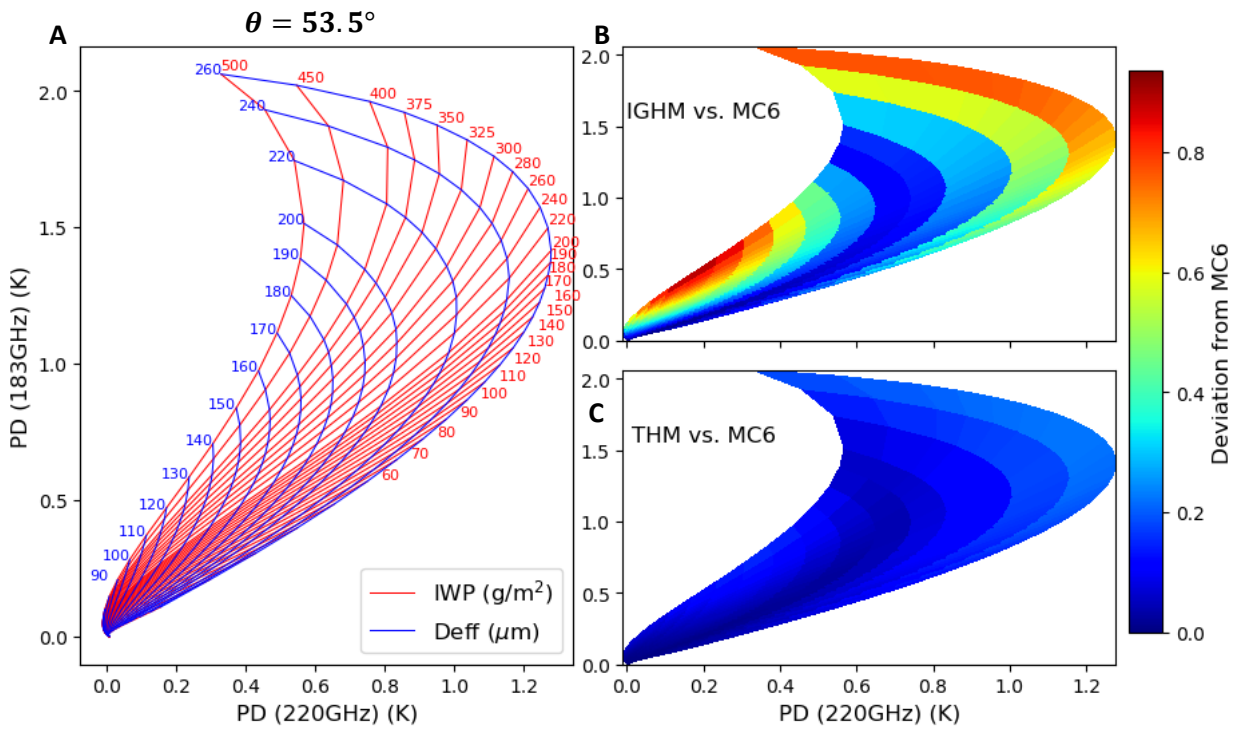

Figure 18. (A) MC6 IWP (red lines) and D_{eff} (blue lines) isoline LUT plots of 183 GHz PDs with respect to 220 GHz PDs for the 53.5° viewing angle. (B) Contour plot of IGHM unit deviation from MC6 fitted in between the LUT isolines of (A). (C) Contour plot of IGHM unit deviation from MC6 fitted in between the LUT isolines of (A).

The 12 µm PD vs. 220 GHz ΔT_b LUT (Figure 19A) was created due to the consistent increase of 12 µm PD values and 220 GHz ΔT_b values with increasing D_{eff} and the large range of PD and ΔT_b values covered by the ice cloud cases. There is decent separation of the isolines for nearly all IWPs and D_{eff}s > 100 µm with IWP and D_{eff} isoline compression occurring when D_{eff}s < 100 µm. This indicates that the 12 µm PD vs. 220 GHz ΔT_b LUT has the potential to accurately retrieve a wide range of IWPs and D_{eff}s with the exception of small D_{eff}s and corresponding IWPs. The IGHM deviation from MC6 are greatest (> 4.0) for IWPs > 150 gm^{-2} and D_{eff}s > 200 µm (Figure 19B).

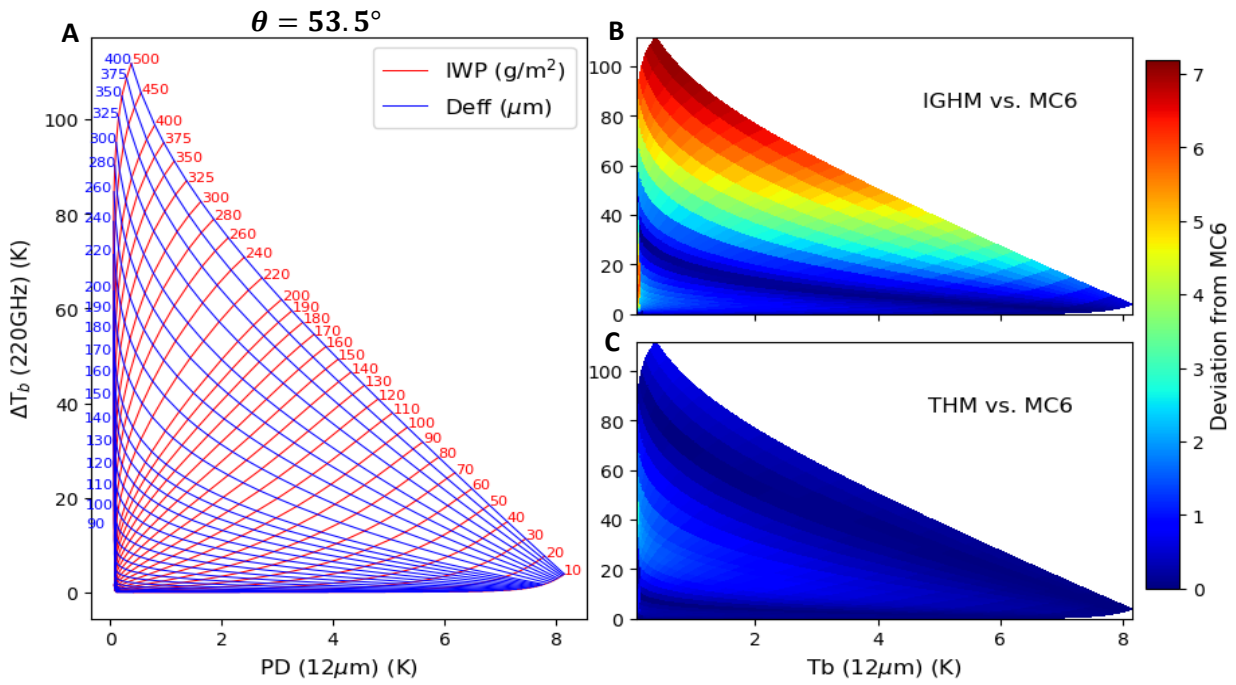

Figure 19. (A) MC6 IWP (red lines) and D_{eff} (blue lines) isoline LUT plots of 220 GHz ΔT_bs with respect to 12 µm PDs for the 53.5° viewing angle. (B) Contour plot of IGHM unit deviation from MC6 fitted in between the LUT isolines of (A). (C) Contour plot of IGHM unit deviation from MC6 fitted in between the LUT isolines of (A).

The THM deviation are in close agreement (< 2.0) with the MC6 LUT for all values of IWPs and D_{eff}s (Figure 19C).

5.1.7. The Case of 424 GHz (669 µm)

The 424 GHz (669 µm) frequency is a peculiar case as it provided extremely low ΔT_bs and PDs rates of change (Figure 20A and 20E) and magnitudes (Figure 20D and 20H) compared to the other wavelengths used for this study regardless of habit mixture. This is due to 424 GHz being primarily sensitive to O_2 (oxygen) allowing the frequency to be used for temperature profiling (Prigent et al. 2006). Even though 424 GHz is somewhat sensitive to ice clouds, it is not on the scale that would be useful for simultaneous IWP and D_{eff} retrievals and thus was not used in the construction of the LUTs.

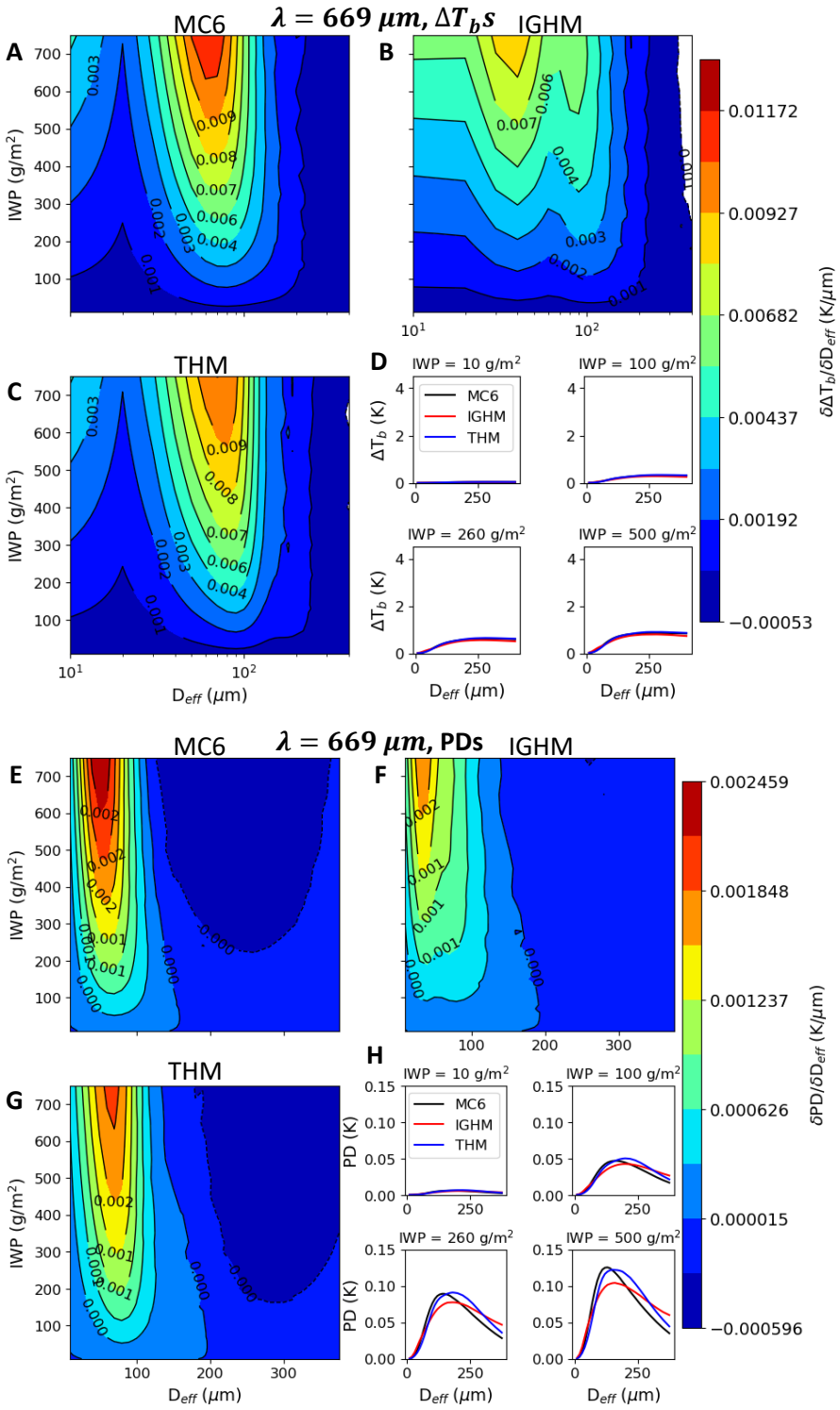

Figure 20. Contour and line plot sets representing sensitivities of 424 GHz (669 μm) ΔT_bs (A – D) and PDs (E – H) with respect to IWP and D_{eff} at the 53.5° viewing angle. (A, E), (B, F), and (C, G) are contour plots displaying $\delta\Delta T_b/\delta D_{eff}$ and $\delta PD/\delta D_{eff}$ for MC6, IGHM, and THM. (D, H) are D_{eff} vs. ΔT_b and D_{eff} vs. PD plots for IWPs of 10 gm^{-2}, 100 gm^{-2}, 260 gm^{-2}, and 500 gm^{-2}.

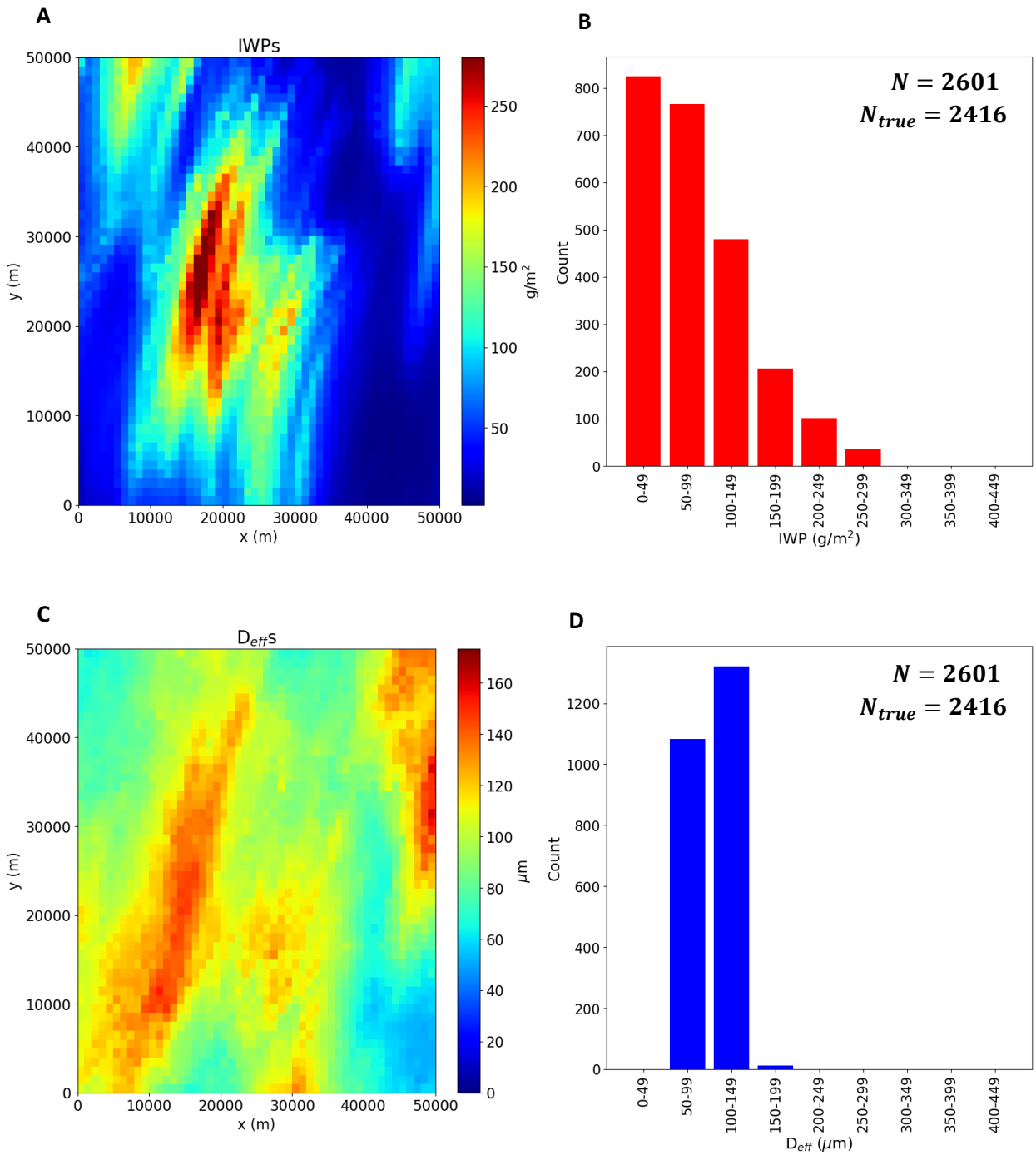

Figure 21. (A) IWPs for the Cloudgen retrieval scenario with each pixel representing a 1 km by 1 km square and a single retrieval case. (B) IWP distribution bar graph with each bar representing a 50 gm^{-2} interval. (C) D_{eff}s for the Cloudgen retrieval scenario with each pixel representing a 1 km by 1 km square and a single retrieval case. (D) D_{eff} distribution bar graph with each bar representing a 50 μm interval. *N* represents the total number of retrieval cases while N_{true} represents the number of retrieval cases considered for analysis due IWPs > 10 gm^{-2} and D_{eff} > 10 μm.

5.2. 2D LUT Retrieval Results

5.2.1. Cloudgen Case IWP and D_{eff} Statistics

Figures 21A and 21C shows the 2D horizontal cloud structure containing IWPs and D_{eff}s for each pixel. Each pixel corresponds to a single retrieval case with a total of 2601 pixels. However, pixels with IWP > 10 gm^{-2} and D_{eff}s > 10 μm were considered for the retrieval analysis. This reduced the total number of retrieval cases to 2416. Cloudgen appeared to give less variability to D_{eff}s as seen in Figure 21D compared to IWPs. This is due to Cloudgen considering D_{eff}s are increasing in size at lower altitudes due to the higher temperatures. The 53.5° viewing angle LUTs from Figures 9A (8.6 μm – 12 μm BTD vs. 12 μm T_b), 14A (220 GHz/183 GHz ΔT_b ratio vs. 680 ΔT_b), 18A (220 GHz PD vs. 183 GHz PD), and 19A (12 μm PD vs 220 GHz ΔT_b) were used to perform the simultaneous IWP and D_{eff} retrievals.

5.2.2. 8.6 μm – 12 μm BTD vs. 12 μm T_b LUT Retrieval Analysis

As discussed in section 5.1.2., the 8.6 μm – 12 μm BTD vs. 12 μm T_b LUT (Figure 9A) had great isoline separation for small values of IWPs (< 70 gm^{-2}) and D_{eff}s (< 50 μm) and then rapidly compressed as the parameters increased. The effects of this can be seen in the retrieval scatterplots of Figure 22A and 22B. In Figure 21A, as true IWP increases (> 50 gm^{-2}), the accuracy of the retrievals decreases and becomes increasingly variable. This resulted in an IWP standard deviation of 151.04 gm^{-2} and a mean percent error of 76.7%. According to Figure 22B, the LUT generally overestimates D_{eff} along with being inconsistent with retrievals. This resulted in a standard deviation of 102.3 μm and a mean percent error of 76.2%. The inaccurate D_{eff} retrievals are likely due to the corresponding large true IWPs which would likely decrease the retrieval accuracy by being within the region of compressed isolines.

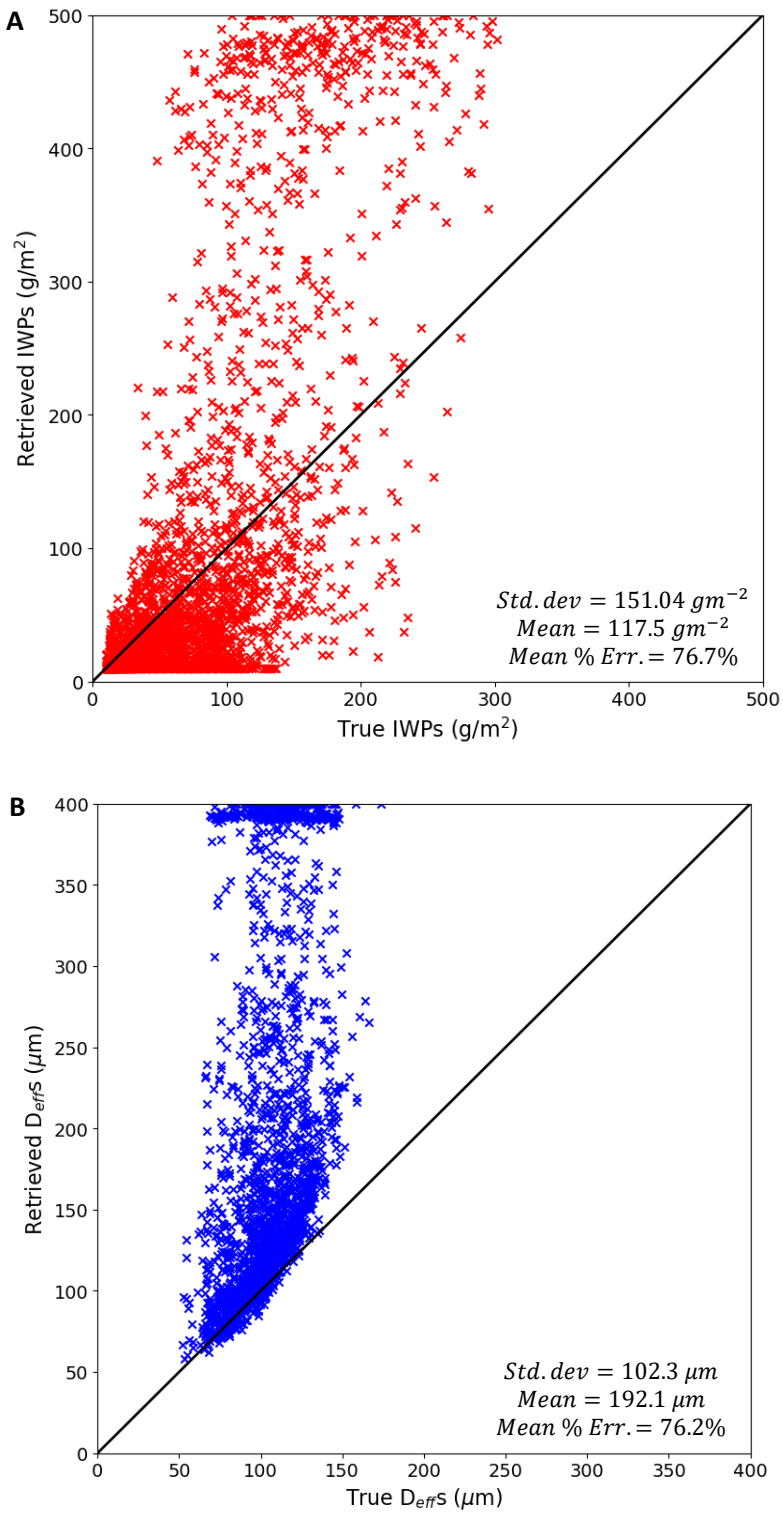

Figure 22. IWP (A) and D_{eff} (B) scatter plots of each retrieval case corresponding to the true values and the retrieved values from the 8.6 µm – 12 µm BTD vs. 12 µm T_b LUT (Figure 9A). *Std. dev* represents the standard deviation of the retrievals and *mean % err.* represents the average percentage error of the D_{eff} retrievals. The black diagonal line represents the line of 0% retrieval error.

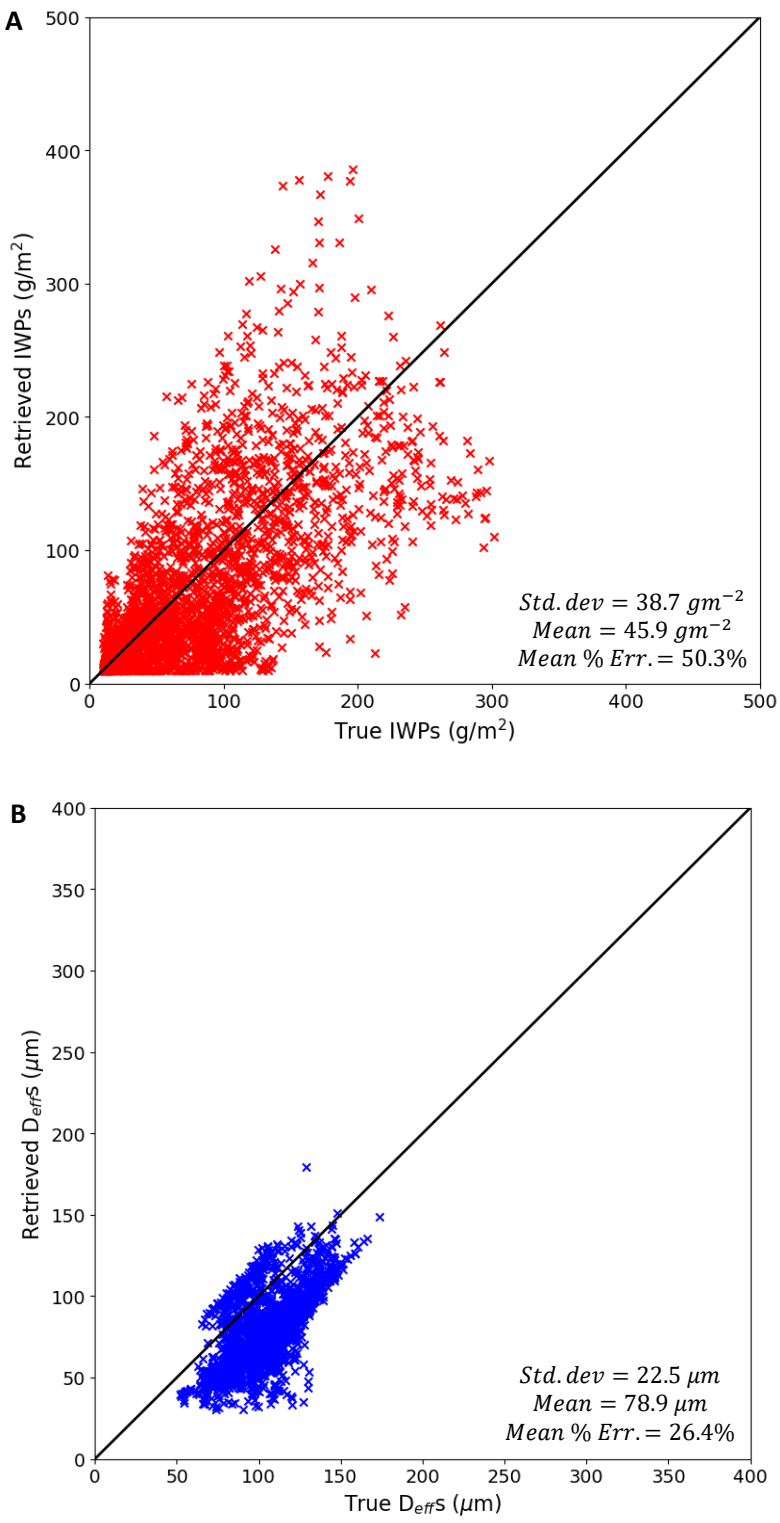

Figure 23. IWP (A) and D_{eff} (B) scatter plots of each retrieval case corresponding to the true values and the retrieved values from the 220 GHz/183 GHz ΔT_b ratio vs. 680 ΔT_b LUT (Figure 14A). *Std. dev* represents the standard deviation of the retrievals and *mean % err.* represents the average percentage error of the retrievals. The black diagonal line represents the line of 0% retrieval error.

Overall, despite showing the potential to accurately retrieve small values of IWP and D_{eff}, LWIR BTDs rapidly becomes unreliable for retrieving moderate and large values of IWP and D_{eff}.

5.2.3. 220 GHz/183 GHz ΔT_b ratio vs. 680 ΔT_b LUT Retrieval Analysis

As discussed in section 5.1.4., the 220 GHz/183 GHz ΔT_b ratio vs. 680 ΔT_b LUT (Figure 14A) had decent IWP and D_{eff} isoline separation for D_{eff}s > 100 μm but IWPs became severely compressed for D_{eff}s < 100 μm while D_{eff} isolines were greatly separated. Due to a majority of true D_{eff}s being less than 150 μm (Figure 21D), the IWP retrievals (Figure 23A) are slightly inaccurate with a mean percent error of 50.3%. The IWP retrievals, however, remain fairly consistent relative to the true values with a standard deviation of 38.7 gm^{-2}. D_{eff} retrievals (Figure 23B), however, are fairly accurate and consistent with a mean percent error of 26.4% and a standard deviation of 22.5 μm. Overall, these results shows the potential of using mm/sub-mm ΔT_bs to simultaneously retrieve a large range of IWPs and D_{eff}s with decent accuracy.

5.2.4. 220 GHz PD vs. 183 GHz PD LUT Retrieval Analysis

As discussed in section 5.1.6., 220 GHz PD vs. 183 GHz PD LUT (Figure 18A) had decent isoline separation for IWPs > 200 gm^{-2} and D_{eff} > 150 μm but becomes more compressed as both parameters decrease, eventually converging to a PD of 0 K for both frequencies. Due to a majority of true D_{eff}s being less than 150 μm, the retrieved IWPs (Figure 24A) are largely inaccurate and inconsistent with a mean percent error of 272.4% and a standard deviation of 164.1 gm^{-2}. Some retrieved IWPs reach a maximum of 500 gm^{-2} despite none of the true IWPs reaching that value. This is likely due to some of the retrieval cases having 183 GHz and 220 GHz PDs being located outside the isolines of the LUT.

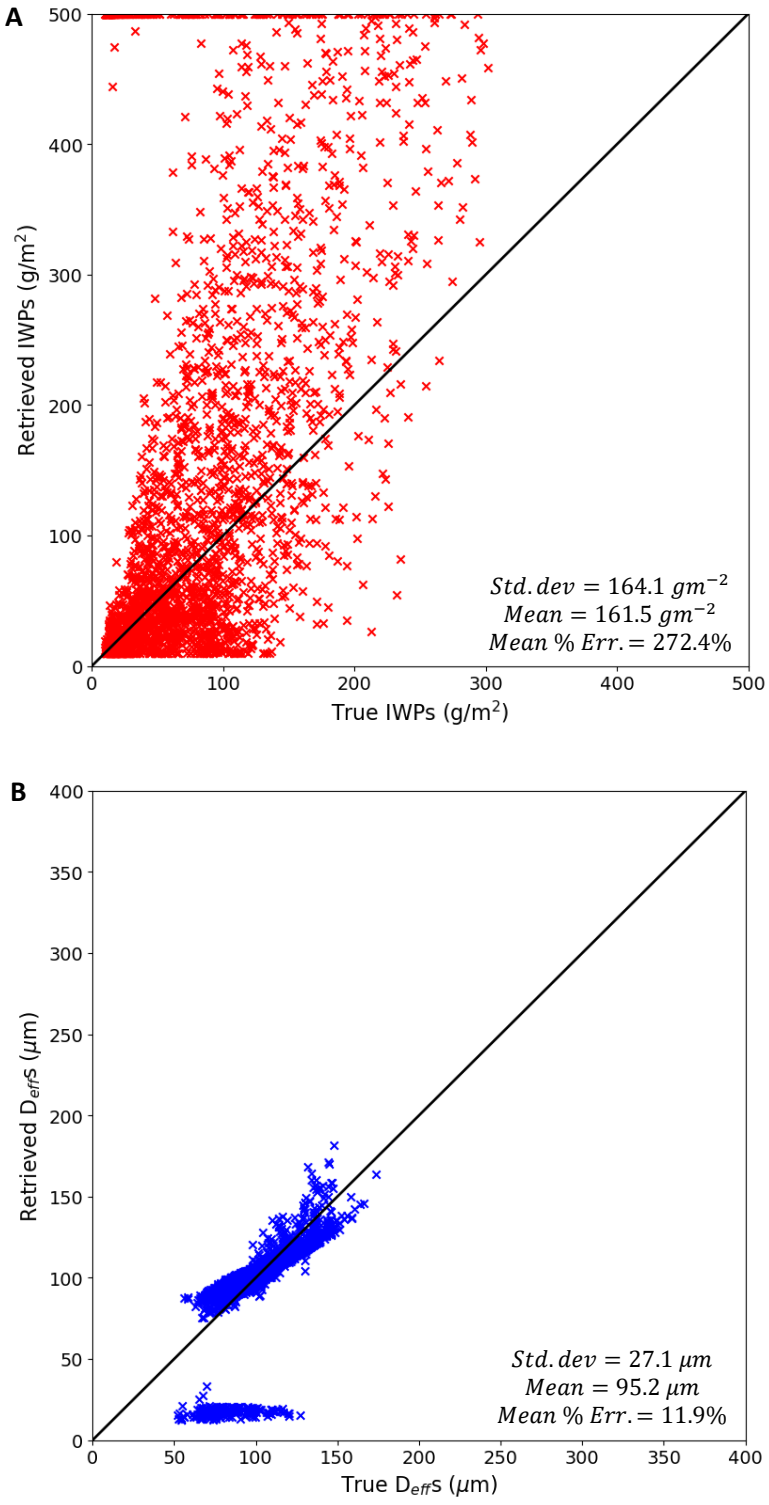

Figure 24. IWP (A) and D_{eff} (B) scatter plots of each retrieval case corresponding to the true values and the retrieved values from the 220 GHz PD vs. 183 GHz PD LUT (Figure 18A). *Std. dev* represents the standard deviation of the retrievals and *mean % err.* represents the average percentage error of the retrievals. The black diagonal line represents the line of 0% retrieval error.

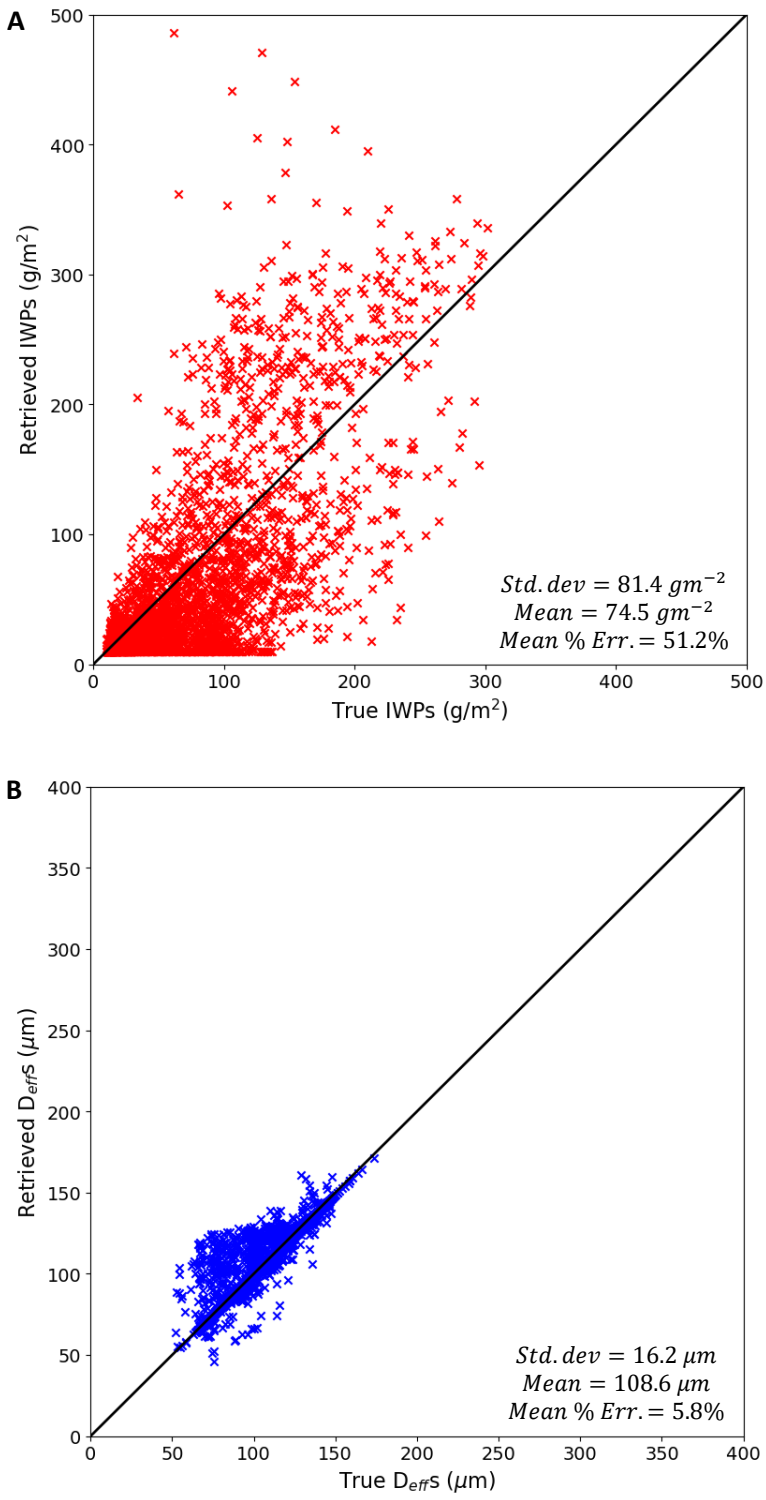

Figure 25. IWP (A) and D_{eff} (B) scatter plots of each retrieval case corresponding to the true values and the retrieved values from the 12 μm PD vs 220 GHz ΔT_b LUT (Figure 19A). *Std. dev* represents the standard deviation of the retrievals and *mean % err.* represents the average percentage error of the retrievals. The black diagonal line represents the line of 0% retrieval error.

Since no IWP and D_{eff} extrapolations outside the LUT were conducted in this study, cases located outside the LUT either have retrieved IWPs and D_{eff}s of the minimum (10 gm^{-2} and 10 μm) or maximum value (500 gm^{-2} and 400 μm). Despite the large inaccuracies of IWP retrievals, the D_{eff} retrievals are very accurate and consistent with a mean percent error of 11.9% and standard deviation of 27.1 μm. The D_{eff} retrievals, however, are separated into two distinct groups with one group having very accurate and precise retrievals and another group of retrievals that underestimates D_{eff} (Figure 24B). The group of retrievals that underestimates D_{eff} mainly have retrieved values of 10 μm. These retrieval cases are likely related to the retrieved IWP cases that reached the maximum value of 500 gm^{-2} which means that the retrieved D_{eff}s have reached the minimum value due to the cases being located outside the LUT. Overall, these results show that using the PDs of the lowest mm/sub-mm frequencies have the potential of simultaneously retrieving IWPs and D_{eff}s, primarily moderate and large values of the parameters.

5.2.5. 12 μm PD vs 220 GHz ΔT_b LUT Retrieval Analysis

As discussed in section 5.1.6., 12 μm PD vs 220 GHz ΔT_b LUT (Figure 19A) had decent isoline separation for D_{eff}s > 100 μm and nearly all IWPs but both IWP and D_{eff} isolines were compressed for ice cloud cases where D_{eff} < 100 μm. Due to a majority of true D_{eff}s being less than 150 μm, the IWP retrievals are slightly inaccurate with a mean percent error of 51.2% (Figure 25A). The IWP retrievals are generally inconsistent relative to the true values with a standard deviation of 81.4 gm^{-2}. Despite the slight inaccuracies of the IWP retrievals and the relatively low true D_{eff}s (Figure 21D), the retrieved D_{eff}s are shown to be very accurate and precise with a mean percent error of 5.8% and standard deviation of 16.2 μm (Figure 25B). As true D_{eff} decreases, the inaccuracies become slightly more apparent due to the D_{eff} isoline compression of the LUT. Although the IWP retrievals are slightly inaccurate, the 12 μm PD vs

220 GHz ΔT_b LUT demonstrates the potential of using different brightness temperature parameters to retrieve ice cloud parameters and opens up the possibility of using numerous combinations to perform accurate retrievals.

6. SUMMARY AND CONCLUSIONS

6.1. Summary

The LWIR wavelengths of 8.6 μm, 10.6 μm, and 12 μm and the mm/sub-mm wavelengths of 440.87 μm (680 GHz), 707.06 μm (424 GHz), 922.44 μm (325 GHz), 1362.69 μm (220 GHz), and 1638.21 μm (183 GHz) were evaluated in their feasibility to retrieve the ice cloud parameters of IWP and D_{eff} by conducting radiative transfer simulations. The results produced by a series of sensitivity analyses, 2D IWP and D_{eff} LUTs, and IWP and D_{eff} retrievals were used as determining factors on whether the wavelengths could be useful for retrieving ice cloud information. 1D simulations of an idealistic 2 km thick ice cloud were conducted through ARTS for the sensitivity analyses and 2D LUT creation. 1D simulations using 3D realistic ice clouds generated by Cloudgen were also conducted through ARTS. The realistic cloud simulations along with the 2D LUTs were used to perform the IWP and D_{eff} retrievals. The sensitivity analyses were initially conducted that used the brightness temperature parameters of the split-window technique (BTD), brightness temperature depression from clear-sky (ΔT_b), and the polarization difference (PD). Three ice particle habit mixtures: MODIS Collection-6 (MC6), the Improved General Habit Mixture (IGHM), and a Two-Habit Model (THM), were used to see whether the use of different particle mixtures would affect the sensitivities of wavelengths to IWP and D_{eff}. The habit mixture of primary focus was MC6. The information gleaned from the sensitivity analyses were then used to create 2D LUTs using isolines of IWPs and D_{eff}s and were analyzed for their potential to simultaneously retrieve IWP and D_{eff}.

6.2. Conclusions

6.2.1. Habit Mixture Effects

The IGHM displayed the most significant disagreements in BTD, ΔT_b, and PD measurements and sensitivities when compared to MC6. The disagreements were more apparent for PDs which was expected since PD is sensitive to particle aspect ratio. The THM displayed general agreements in BTD and ΔT_b measurements and sensitivities but noticeable disagreements in PD when compared to MC6. This demonstrates how ice cloud parameter retrievals could possibly be affected through the use of different habit mixtures despite being realistic representations of ice particle concentrations within observed ice clouds.

6.2.2. MC6 IWP and D_{eff} Sensitivities and Retrievals

8.6 μm – 10.6 μm and 8.6 μm – 12 μm BTD sensitivities rapidly decreased as IWP and D_{eff} increased. An 8.6 μm – 12 μm BTD LUT was created to perform retrievals due to the higher BTD magnitudes compared to 8.6 μm – 10.6 μm. IWP retrievals decreased in accuracy as true IWPs increased due to the BTD insensitivity to large IWPs. D_{eff} retrievals were generally inaccurate as a majority of true D_{eff}s were greater than 100 μm. Overall, LWIR split-window BTDs appear to be only useful for accurately retrieving IWPs and D_{eff}s from ice clouds having very small ice particles and IWP. Perhaps if retrievals were restricted to only thin cirrus then the split-window BTDs would be effectively utilized.

Mm/sub-mm ΔT_b sensitivities increased as IWP and D_{eff} increased. For higher mm/sub-mm frequencies (lower wavelengths), ΔT_b sensitivities shifted to lower D_{eff}s which meant that mm/sub-mm frequencies contained ice particle size information. A 220 GHz/183 GHz ΔT_b ratio vs. 680 GHz ΔT_b LUT was created to perform retrievals due to the ΔT_b ratio containing ice particle size information and 680 GHz being sensitive to a large range of D_{eff}s that was used in

this study. IWP retrievals were overall slightly inaccurate, especially for large IWPs, but precise relative to true IWP values while D_{eff} retrievals were generally accurate and precise. Overall, mm/sub-mm ΔT_bs have the potential to retrieve a large range of IWPs and D_{eff}s with higher frequencies being more useful for retrieving relatively small D_{eff}s.

Mm/sub-mm PD sensitivities generally increased as IWP and D_{eff} increased but there was a pronounced resonance feature present in the PD calculations especially for that higher frequencies (lower wavelengths). The resonance feature did noticeably shift to smaller D_{eff}s as sub-mm/mm frequency increases which means that the resonance feature contains particle size information. However, the resonance feature has the potential to complicate simultaneous IWP and D_{eff} retrievals due to two different D_{eff} values possibly having the same PD value. A 220 GHz vs. 183 GHz PD LUT was created to perform retrievals due to the lack of a prominent resonance feature for the lowest mm/sub-mm frequencies. IWP retrievals were very inaccurate due to a noticeable amount of cloud cases having 220 GHz and 183 GHz PDs corresponding to values that lie outside the outermost isolines of the LUT. Despite this, the D_{eff} retrievals showed to be very accurate and precise. There was however a peculiar separation of the D_{eff} retrievals. The less accurate retrieval group were mainly concentrated at around 10 μm meaning that they most likely were the same cloud cases that had PD values lying outside the LUT. Overall, the lowest mm/sub-mm frequency (largest wavelengths) PDs have the potential to retrieve IWP and D_{eff}. Perhaps a different retrieval method could be implemented to utilize the PD resonance feature as it contains particle size information and could lead to more accurate D_{eff} retrievals and could even lead to more accurate IWP retrievals.

LWIR PD sensitivities were greatest for small IWPs and small to moderate D_{eff}s. Unlike the presence of a resonance feature for the mm/sub-mm wavelengths, there was a consistent

increase in PD as D_{eff} increased with the greatest magnitudes being calculated for 12 μm. A 12 μm PD vs. 220 GHz ΔT_b LUT was created to perform retrievals due to the wavelengths containing consistent increases in PDs and ΔT_bs as D_{eff} increased. The IWP retrievals were slightly inaccurate but precise while D_{eff} retrievals were among the most accurate and precise than all the other LUTs. This shows that using combinations of LWIR and mm/sub-mm along with combinations of brightness temperature parameters can have the potential to accurately retrieve IWP and D_{eff} along with other ice cloud parameters such as optical thickness. Satellite-borne instruments that operates with wavelengths within the LWIR and mm/sub-mm regimes will be able to perform this task and thus allow for the better understanding of the radiative properties of ice clouds.

REFERENCES

Baum, B. A., P. Yang, A. J. Heymsfield, C. Schmitt, Y. Xie, A. Bansemer, Y.-X. Hu, and Z. Zhang, 2011: Improvements to shortwave bulk scattering and absorption models for the remote sensing of ice clouds. *J. Appl. Meteor. Clim.*, **50**, 1037 – 1056. **© American Meteorological Society. Used with permission.**

Buehler, S., C. Emde, P. Eriksson, O. Lemke, 2017: Atmospheric Radiative Transfer Simulator (ARTS) User Guide.

Davis, C. P., K. F. Evans, S. A. Buehler, D. L. Wu, and H. C. Pumphrey, 2007: 3-D polarized simulations of space-borne passive mm/sub-mm midlatitude cirrus observations: a case study. *Atmospheric Chemistry and Physics*., **7**, 4149 – 4158.

Dubuisson, P., V. Giraud, J. Pelon, B. Cadet, P. Yang, 2008: Sensitivity of Thermal Infrared Radiation at the Top of the Atmosphere and the Surface to Ice Cloud Microphysics. *Journal of Applied Meteorology and Climatology*., **47**, 2545 – 2559.

Emde, C., S. A. Buehler, C. Davis, P. Eriksson, T. R. Sreerekha, and C. Teichmann, 2004: A polarized discrete ordinate scattering model for simulations of limb and nadir longwave measurements in 1D/3D spherical atmospheres. *Journal of Geophysical Research*, **109**.

Evans, K. F., and G. L. Stephens, 1995a: Microwave Radiative Transfer through Clouds Composed of Realistically Shaped Ice Crystals. Part I: Single Scattering Properties. *Journal of the Atmospheric Sciences.*, **52**, 2041 – 2057.

Evans, K. F., and G. L. Stephens, 1995b: Microwave Radiative Transfer through Clouds Composed of Realistically Shaped Ice Crystals. Part II: Remote Sensing of Ice Clouds. *Journal of the Atmospheric Sciences.*, **52**, 2058 – 2072.

Evans, K. F., S. J. Walter, A. J. Heymsfield, G. M. McFarquhar, 2002: Submillimeter-Wave Cloud Ice Radiometer: Simulations of retrieval algorithm performance. *Journal of Geophysical Research: Atmospheres*., **107, D3**, 2-1 – 2-21.

Fauchez, T., P. Dubuisson, C. Cornet, F. Szĉzap, A. Garnier, J. Pelon, and K. Meyer, 2015: Impacts of cloud heterogeneities on cirrus optical properties retrieved from space-based thermal infrared radiometry. *Atmospheric Measurement Techniques*., **8**, 633 – 647.

Feofilov, A. G., C. J. Stubenrauch, and J. Delanoë, 2015: Ice water content vertical profiles of high-level clouds: classification and impact on radiative fluxes. *Atmospheric Chemistry and Physics*., **15**, 12327 – 12344.

Hogan, R. J., and S. F. Kew, 2005: A 3D stochastic cloud model for investigating the radiative properties of inhomogeneous cirrus clouds. *Q. J. R. Meteorol. Soc.*, **131**, 2585 – 2608

Inoue, T., 1985: On the temperature and effective emissivity determination of semi-transparent cirrus clouds by bi-spectral measurements in the window region. *J. Meteor. Soc. Japan*. **63**, 88 – 98.

Iwabuchi, H., and P. Yang, 2011: Temperature dependence of ice optical constants: Implications for simulating the single-scattering properties of cold ice clouds. *J. Quant. Spectrosc. Radiat. Transfer*, **112**, 2520 – 2525.

J. Miao, K.-P. Johnsen, S. Buehler, A. Kokhanovsky, 2003: The potential of polarization measurements from space at mm and sub-mm wavelengths or determining cirrus cloud parameters. *Atmospheric Chemistry and Physics*., **3**, 39 – 48.

Liou, K. N., 1986: Influence of cirrus clouds on weather and climate processes: a global perspective. *Monthly Weather Review*., **114**, 1167 – 1199.

Liu, C., P. Yang, P. Minnis, N. Loeb, S. Kato, A. Heymsfield, C. Schmitt, 2014: A two-habit for the microphysical and optical properties of ice clouds. *Atmospheric Chemistry and Physics*. **14**, 13719-13737.

Liu, G., J. A. Curry, 2000: Determination of Ice Water Path and Mass Median Particle Size Using Multichannel Microwave Measurements. *Journal of Applied Meteorology*. **39**, 1318 – 1329.

Platnick, S., M. D. King, K. G. Meyer, G. Wind, N. Amarasinghe, B. Marchant, G. T. Arnold, Z. Zhang, P. A. Hubanks, B. Ridgway, and J. C. Riedi, 2015: MODIS cloud optical properties: User guide for the collection 6 level-2 MOD06/MYD06 product and associated level-3 datasets. Version 1.0, 141 pp.

Prabhakara, C., R. S. Fraser, G. Dalu, M.-L. C. Wu, R. J. Curran, and T. Styles, 1988: Thin cirrus clouds: Seasonal distribution over oceans deduced from Nimbus-4 IRIS. *Journal of Applied Meteorology and Climatology*, **27**, 379 – 399.

Shaw, J. A. and P. W. Nugent, 2013: Physics principles in radiometric infrared imaging of clouds in the atmosphere. *European Journal of Physics*., **34**, S111 – S121.

Wang, C., P. Yang, B. A. Baum, S. Platnick, A. K. Heidinger, Y. Hu, R. E. Holz, 2011: Retrieval of Ice Cloud Optical Thickness and Effective Particle Size Using a Fast Infrared Radiative Transfer Model. *Journal of Applied Meteorology and Climatology*., **50**, 2283-2297.

Wang P. H., 1996: A 6-year climatology of cloud occurrence frequency from Stratospheric Aerosol and Gas Experiment II observations (1985 – 1990), *J. Geophys. Res.*, **101** (D23), 29407 – 29429.

Weisstein, Eric W, 2019. "Cubic Spline." From MathWorld--A Wolfram Web Resource. http://mathworld.wolfram.com/CubicSpline.html

Weng, F., and N. C. Grody, 2000: Retrieval of ice cloud parameters using a microwave imaging radiometer. *Journal of the Atmospheric Sciences*, **57**, 1069 – 1081.

Wu, D. L., J. Esper, N. Ehsan, T. E. Johnson, W. R. Mast, J. R. Piepmeier, P. E. Racette, 2014: IceCube: Spaceflight Validation of an 874 GHz Submillimeter Wave Radiometer for Cloud Ice Remote Sensing. *Earth Science Technology Forum*. Leesburg, VA, USA, Oct. 28 – 30, 2014. http://esto.nasa.gov/forum/estf2014/presentations/B1P5Wu.pdf

Yang, P., H. Wei, H.-L. Huang, B. A. Baum, Y.X. Hu, G.W. Kattawar, M.I. Mishchenko, and Q. Fu, 2005: Scattering and absorption property database for nonspherical ice particles in the near- through far-infrared spectral region. *Appl. Opt*., **44**, 5512 – 5523.

Yang, P., L. Bi, B.A. Baum, K. N. Liou, G.W. Kattawar, M.I. Mishchenko, and B. Cole, 2013: Spectrally consistent scattering, absorption, and polarization properties of atmospheric ice crystals at wavelengths from 0.2 μm to 100 μm. *Journal of the Atmospheric Sciences*., **70**, 330 – 347.